1	The Roles of Moat Width and Outer Eyewall Contraction in Affecting the
2	Timescale of Eyewall Replacement Cycle
3	Jie Jiang ^{1,2} , and Yuqing Wang ³
4 5	¹ Department of Atmospheric and Ocean Sciences, Institute of Atmospheric Sciences, Fudan University, Shanghai, China
6 7	² State Key Laboratory of Severe Weather, Chinese Academy of Meteorological Sciences, China Meteorological Administration, Beijing, China
8	³ Department of Atmospheric Sciences and International Pacific Research Center, School of Ocean and Earth Science and Technology, University of Hawaii at Manoa, Honolulu, HI, USA
10	<u>April 30, 2024 (submitted)</u>
11	August 5, 2024 (first revision)
12	September 18, 2024 (second revision)
13	Key points
14	1. The boundary layer dynamics by which the moat width regulates the interaction between inner
15	and outer eyewalls is demonstrated/emphasized
16	2. The inner eyewall is supported by greater inward absolute vorticity flux and maintained for a
17	longer time period when a larger moat exists
18	3. Active outer rainbands can slow down the contraction of the outer eyewall and increase the
19	timescale of the eyewall replacement cycle
20	Submitted to <i>Journal of Geophysical Research – Atmospheres</i>

Corresponding author: Prof. Yuqing Wang (yuqing@hawaii.edu)

22 Abstract

The timescale of eyewall replacement cycle (ERC) is critical for the prediction of intensity and structure changes of tropical cyclones (TCs) with concentric eyewall (CE) structures. Previous studies have indicated that the moat width can regulate the interaction between the inner and outer eyewalls and has a salient relationship with the ERC timescale. In this study, a series of sensitivity experiments are carried out to investigate the essential mechanisms resulting in the diversity of the duration of CEs using both simple and full-physics models. Results reveal that a larger moat can induce stronger inflow under the same inner eyewall intensity by providing a longer distance for air parcels to accelerate in the boundary layer. Thus, there is greater inward absolute vorticity flux to sustain the inner eyewall. Besides, the equivalent potential temperature (θ_e) budget indicates that the vertical advection and surface flux of moist entropy can overbalance the negative contribution from the horizontal advection and lead to an increasing trend of θ_e in the inner eyewall. This suggests that the thermodynamic process in the boundary layer is not indispensable to the inner eyewall weakening. It is also found that the contraction rate of the secondary eyewall, which directly influences the moat width, is subject to the activity of outer spiral rainbands. By directly introducing positive wind tendency outside the eyewall and indirectly promoting a vertically tilted eyewall structure, active convection in the outer region will impede or even suspend the contraction of the outer eyewall and hence extend the ERC timescale.

Plain Language Summary: The eyewall replacement cycle (ERC), during which the inner eyewall gradually fades away and is replaced by the outer eyewall ultimately, can impose significant influences on the intensity and structure of tropical cyclones. However, few efforts have been devoted to understanding the timescale of the ERC. The idealized simulations of this study highlight the essential role of the moat width (the radial region between the inner and outer eyewall containing suppressed convection) in the decay rate of the inner eyewall. Results show that a wider moat can provide longer travelling distance for air parcels in the boundary layer to obtain larger radial velocity and to bring greater flux of angular momentum inward, which helps the inner eyewall persist. Besides, stronger diabatic heating rates of outer spiral rainbands tend to slow down the contraction of the outer eyewall by introducing larger positive wind tendency outside than inside the outer eyewall, therefore reducing the contraction rate of the outer eyewall and extending

the ERC timescale.

1. Introduction

Research on the eyewall replacement cycle (ERC) in tropical cyclones (TCs) has progressed over the last few decades (Black & Willoughby, 1992; Fortner, 1958; Samsury & Zipser, 1995; Willoughby, 1990; Willoughby et al., 1982). The importance of ERC to TC structure and intensity changes is manifested in its universality (Hawkins et al., 2006; Hawkins & Helveston, 2004; Kossin & Sitkowski, 2009; Kuo et al., 2009; Sitkowski et al., 2011), and its challenge to TC structure and intensity forecasts (Chen, 2018; Houze et al., 2007; Rozoff et al., 2008; Sitkowski et al., 2011; Wu et al., 2012; Zhou et al., 2011). The formation of the outer (secondary) eyewall outside the inner (primary) eyewall is always accompanied by the broadening of the wind field, which can increase the total energy of TCs and the potential damage to the human society (Irish et al., 2008; Lin et al., 2014). In general, the ERC process consists of the secondary eyewall formation (SEF; Abarca & Corbosiero, 2011; Abarca & Montgomery, 2013, 2014; Abarca et al., 2015; Ahern et al., 2022; Huang et al., 2012; Kepert, 2013; Kepert & Nolan, 2014; Kuo et al., 2008; Kuo et al., 2004; Qiu et al., 2010; Rozoff et al., 2006; Terwey & Montgomery, 2008), contraction and intensification of the outer eyewall along with weakening of the inner eyewall, and replacement of the inner eyewall by the outer eyewall.

Although Kuo et al. (2009) reported that more than half of the ERC cases follow the typical paradigm, namely increases (decreases) of TC intensity before (after) the SEF, there exist nonnegligible examples of unique evolution of concentric eyewalls (CEs). In terms of intensity change, the secondary eyewall does not necessarily form at the intensification phase of a TC and does not always indicate the weakening of TC intensity either (Kuo et al., 2009; Willoughby et al., 1982). In a CE configuration, on the one hand, suspension of eyewall replacement can happen when the outer eyewall disappears or both inner and outer eyewalls dissipate simultaneously due to environmental wind shear or topography (Hawkins, 2008; Zhu & Yu, 2019); on the other hand, multiple ERC events and triple eyewalls are documented based on observations (McNoldy, 2004; Molinari et al., 2019; Wang et al., 2023; Zhao et al., 2016). Besides, the timescale for a TC to complete an ERC also varies greatly. The average CE duration in the western North Pacific and the North Atlantic is 16 h and 10 h but there are 12% and 6% ERC events that endure more than 30 hours, respectively (Yang et al., 2021). The diversity of ERC patterns motivates us to study the

internal dynamics and environmental conditions that are responsible for those distinct characteristics among CEs, and the variability of ERC timescale is of special interest as it currently presents the largest TC intensity prediction barrier (Chen et al., 2023). During a general ERC event, TC evolution is subject to the mutual interaction between the inner and outer eyewalls, in contrast to a single-eyewall phase. Therefore, predicting the end of an ERC is of the same importance as knowing the timing of SEF.

TCs with long-lived CEs are especially concerned due to their persistently large areal coverage of damaging winds and have been studied extensively in the literature (Tsujino et al., 2017; Wang et al., 2023; Yang et al., 2014). Based on passive microwave satellite imagery from 1997 to 2011 in the western North Pacific, Yang et al. (2013) found that CE structures that can sustain for more than 20 hours generally have larger TC intensity, moat width and outer eyewall width at the time of SEF than those of shorter duration. More recently, using an extended satellite dataset, Yang et al. (2021) further investigated the relationship between CE duration and structural parameters of CEs in the western North Pacific, the North Atlantic, and the eastern North Pacific. They revealed that the ERC timescale is noticeably correlated to moat width and outer eyewall width in all three basins, but its relationships with inner eyewall intensity and inner-core size are less significant.

As summarized in Kuo et al. (2009), for TCs that follow the classical ERC paradigm, the ERC timescale is directly influenced by the decay rate of the inner eyewall. Therefore, it is important to understand underlying mechanisms that cause the weakening of the inner eyewall. There are numerous studies on this issue from the viewpoint of internal dynamics, and interestingly most of them interpret the collapse of the inner eyewall in a way that the moat width can decide the pace. Yang et al. (2013) speculated that the type-2 barotropic instability (Kossin et al., 2000; Rozoff et al., 2008), which can mix potential vorticity across the moat and distort eyewall structures, is more likely to emerge when the moat is narrow. Lai et al. (2019) argued that the excitation of wavenumber-2 (WN-2) vortex Rossby waves at lower levels of the simulated hurricane Wilma (2005) sharply led to the breakdown of the inner eyewall. The outward eddy radial transport of eddy absolute angular momentum across the moat induced by the wave instability can result in the dissipation of the inner eyewall and enhancement of the outer eyewall (Lai, Hendricks, Menelaou, & Yau, 2021; Lai, Hendricks, & Yau, 2021; Lai, Hendricks, Yau, & Menelaou, 2021; Rostami & Zeitlin, 2022). Elliptic inner eyewall structures near the end of ERCs have been documented in observations like in typhoon Trami (2018) (Tsujino et al., 2021) and hurricane Maria (2017)

(Slocum et al., 2023), supporting the argument that the type-2 barotropic instability can significantly contribute to the demise of the inner eyewall.

From the axisymmetric perspective, Willoughby et al. (1982) suggested that the upper-level divergent flow of the outer eyewall could counteract the inner eyewall's outflow. Willoughby et al. (1982) and Willoughby (1990) proposed that the subsidence induced by the outer eyewall convection could disrupt the inner eyewall updraft. Zhu and Zhu (2014) confirmed that as the moat width shortens and the outer eyewall strengthens the descending branch of the outer eyewall' transverse circulation would cover most the TC inner-core region and suppress convection in the inner eyewall according to the balanced vortex dynamics. However, this was not supported by the result of Rozoff et al. (2008), who derived an analytic solution, showing that the downdraft introduced by the outer eyewall is mainly confined to the moat and eye regions and argued that the dissipation of the inner eyewall arises from the enhanced inner-core static stability.

Considering the key role of the boundary layer played in the TC development, the interception of inward moist entropy and momentum fluxes by the outer eyewall is generally believed detrimental to the inner eyewall. Zhou and Wang (2011) indicated that the outer eyewall in a TC with enhanced ice concentrations tends to form at a larger radius and blocks the supply of moist entropy in a less effective way. On the contrary, a TC wherein the outer eyewall is close to the center has an obvious transport of low moist entropy into the inner eyewall and experiences quick eyewall replacement due to a sharper negative gradient of equivalent potential temperature (θ_e) in the moat. Based on the numerical simulation of the long-lived Typhoon Bolaven (2012), Tsujino et al. (2017) found that the positive θ_e tendency in the TC inner core is sufficient for the survival of the inner eyewall although the moist entropy supply was reduced after the SEF. However, they also cautioned that it is unclear whether the θ_e tendency in the inner core becomes zero or negative in short-lived CEs.

The convective barrier can prohibit inward angular momentum transfer due to the buoyancy-driven consumption of air masses (Houze et al., 2007; Samsury & Zipser, 1995). Kuo et al. (2022) proposed a dimensionless scaling law for the inner eyewall pumping based on a forced slab boundary layer model. They indicated that the inner eyewall updraft scaled with the maximum wind speed is positively proportional to the moat width scaled with the Rossby deformation radius and proposed that the maintenance of the inner eyewall is governed by the pressure gradient force that accelerates inflow within the moat region. Although Kuo et al. (2022) discussed how the

boundary layer dynamical process may contribute to the inner eyewall decay, the use of a model without coupling between the boundary layer and the free atmosphere hindered complete verification of their hypothesis. Therefore, we will examine the boundary layer mechanism in a time-evolving framework in terms of the decay rate rather than assuming the steady state of the inner eyewall as in Kuo et al. (2022).

In spite of many studies on inner eyewall dissipation mechanisms, fewer of them have probed into the issue of outer eyewall contraction which is connected to the change rate of the moat width and thus the dissipation of the inner eyewall and the timescale of the ERC in TCs. Abarca and Montgomery (2015) emphasized the dominant role of the boundary layer in spinning up swirling winds at radially inward side of the secondary eyewall. Chen (2018) suggested that an outer eyewall can shrink swiftly when there exists strong boundary layer inflow. Besides, Tsujino et al. (2017) illustrated that both the axisymmetric and asymmetric components of potential vorticity generation can contribute to the outer eyewall contraction. In this study, we will show how the activity of outer spiral rainbands impacts the contraction of the outer eyewall and address its connection to the ERC timescale. The rest of article is organized as follows. Section 2 presents a brief description of model configurations and experimental designs of two numerical models including the three-layer Ooyama-type model and the full-physics cloud model CM1. The boundary layer mechanism leading to the demise of the inner eyewall and the relationship between the moat width and the decay rate based on the Ooyama-type model are discussed in section 3. Results from the CM1 model and the connection between the rainband activity and the inward contraction of the outer eyewall are analyzed in section 4. Finally, main conclusions are summarized and discussed in the last section.

2. Model and experimental design

143

144

145

146

147

148

149

150

151

152

153

154

155

156

157

158

159

160

161

162

163

164

165

166

167

168

169

170

171

172

The three-layer Ooyama-type model (OM3L hereafter, Ooyama, 1969; Schecter & Dunkerton, 2009) and the full-physics cloud model CM1 (Bryan & Rotunno, 2009) are used to investigate factors that affecting the timescale of ERC in TCs. Although the OM3L model only consists of minimal parametrizations of cumulus convection and air-sea interaction, previous studies have proved its capability to capture the formation and basic evolution of TCs (cf. Schecter & Dunkerton, 2009). On account of the simplicity of the OM3L model, it is much easier to manipulate the vortex structure while keeping dynamic and thermodynamic variables at different layers coupled.

Although the fundamental dynamics underpinning the CE evolution can be clearly revealed in a simplified framework that is free of complicated physical processes, a more state-of-art model, the CM1 model, is employed to confirm the primary conclusions derived from the OM3L model. Model settings of the two models and parameters of sensitivity experiments are described below.

2.1 The OM3L model

A detailed description of the OM3L model including the governing equations, constants, parameters and parametrization schemes is provided in Schecter and Dunkerton (2009). In brief, the OM3L model is comprised of a slab boundary layer (denoted by subscript b), a lower free atmospheric layer (denoted by subscript 1), and an upper free atmospheric layer (denoted by subscript 2). Momentum and mass fluxes are allowed between any adjacent layers, while keeping the density of each layer constant with the boundary layer of a rigid height of 1 km and the lower and upper free atmospheric layers of changeable depths. Enthalpy and momentum exchanges take place at the interface between the sea surface and the boundary layer. The Ooyama-type cumulus parameterization is deployed, in which the activity of convection is defined by the entrainment parameter η . In contrast to the uncoupled Ooyama-type model used in Kuo et al. (2022), the OM3L model allows for the interaction between the boundary layer and the free atmosphere aloft. The domain covers 3000 km×3000 km area with a grid spacing of 2.5 km. Numerical experiments are performed on an f-plane with the Coriolis parameter of 5×10^{-5} s⁻¹ and a constant sea surface temperature of 29° C. The model is initialized with a prescribed vertical relative vorticity (ξ) profile featuring a CE structure

$$\xi = \begin{cases} \xi_{i}, & r \leq r_{i}, \\ \xi_{i} \cdot \exp\left(-\left(\frac{r - r_{i}}{l_{i}}\right)^{2}\right) + \xi_{o} \cdot \exp\left(-\left(\frac{r - r_{o}}{l_{o}}\right)^{8}\right), & r > r_{i}. \end{cases}$$
 (1)

In the control run, $\xi_i = 4.0 \times 10^{-3} \text{ s}^{-1}$ and $\xi_o = 5.0 \times 10^{-4} \text{ s}^{-1}$ are the maximum vertical vorticities of the inner core and the outer eyewall, respectively; $r_i = 25 \text{ km}$ and $r_o = 100 \text{ km}$ are the radii of the inner core and the central radius of the outer eyewall, respectively; $l_i = 7.5 \text{ km}$ is the length of the transition region from the high inner-core vorticity ξ_i to zero vorticity, and $l_o = 20 \text{ km}$ is the width of the outer eyewall. Those parameters are chosen in reference to the average intensities and sizes of inner and outer eyewalls when the CE structure forms in observations (Sitkowski et al., 2011). Both the boundary layer and the lower free atmosphere in the

OM3L model are driven by the same TC structure, but ξ_i is reduced to the one third of the magnitude and ξ_0 is set to zero in the upper free atmosphere. Observational studies have suggested the significant correlation between the ERC timescale and the moat width (Yang et al., 2013; Yang et al., 2021), thus it is natural to examine different CE evolutions with various moat widths. The tangential wind and vorticity distributions at the time of 0 h in the control run and sensitivity experiments are shown in Figure 1. Structural parameters of sensitivity experiments except for r_0 are kept same as those in the control run. Because the vertical velocity is zero everywhere before the model spins up, the moat width can be estimated as the radial extent of the area where the radial gradient of relative vorticity is non-negative, according to linear Ekman theory (Kepert, 2013). Five sensitivity experiments with different moat widths are carried out to elucidate the essential dynamics facilitating eyewall replacement based on the OM3L model. In the five sensitivity experiments, r_0 is set as 80, 90, 100, 110, and 120 km, respectively. The corresponding experiments are termed as R80, R90, R100, R110, and R120 and discussed in section 3.1. Besides, to clarify and quantify the relationship between the inner eyewall weakening rate and moat width, additional five hundred experiments are conducted by varying structural parameters of CEs. The structural parameters include inner eyewall vorticity (ξ_i =3.4, 3.7, 4.0, 4.3, $4.6 \times 10^{-3} \,\mathrm{s}^{-1}$), outer eyewall vorticity ($\xi_0 = 3.0, 4.0, 5.0, 6.0, 7.0 \times 10^{-3} \,\mathrm{s}^{-1}$), outer eyewall radius $(r_0=80, 90, 100, 110, 120 \text{ km})$, and outer eyewall width $(l_0=10, 20, 30, 40 \text{ km})$. Here, we do not modify the RMW of the inner eyewall (which is termed as r_i) because the impact of RMW is accomplished by influencing the inertial stability, whose change can be realized by varying ξ_i . The quantified relationship will be presented in section 3.2.

201

202

203

204

205

206

207

208

209

210

211

212

213

214

215

216

217

218

219

220

221

222

223

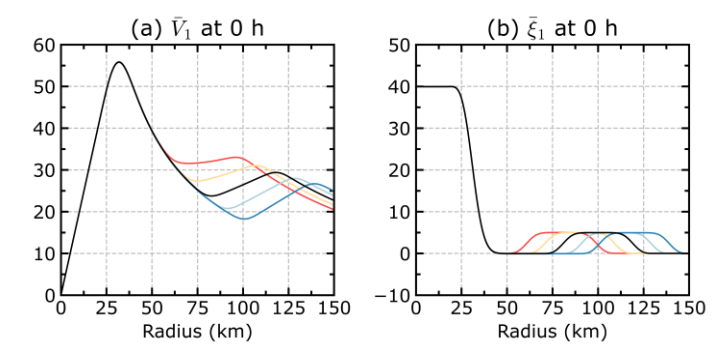


Figure 1. Radial profiles of (a) tangential wind (m s⁻¹) and (b) relative vertical vorticity (× 10⁻⁴ s⁻¹) of the initial vortex in the boundary layer and lower free atmospheric layer used in experiments R80 (red), R90 (yellow), R100 (black), R110 (light blue), and R120 (deep blue).

2.2 The CM1 model

226

227

228

229

230

231

232

233

234

235

236

237

238

239

240

241

242

243

244

245

246

247

248

249

250

251

252

253

The nonhydrostatic and fully compressible full-physics cloud model CM1 of version 21.0 is used to test the robustness of the results from the simple OM3L model. Since this study focuses on the axisymmetric processes that lead to the demise of the inner eyewall, the axisymmetric version of CM1 is applied. The model horizontal resolution is 1 km within the radius of 300 km then linearly stretches to 15 km at the radius of 3500 km (stretch x=2, dx inner=1000.0, $dx \ outer=15000.0, \ nos \ x \ len=300000.0, \ tot \ x \ len=3500000.0)$. There are 60 levels in the vertical, with a grid spacing from 50 m at the lowest level to 500 m at and above 5.5 km (stretch z=1, str bot=0.0, str top=5500.0, dz bot=50.0, dz top=500.0, ztop=25500.0). We deploy the Thompson microphysics scheme (ptype=3, Thompson et al., 2008), the Louis-type planetary boundary layer scheme (ipbl=2, Bryan & Rotunno, 2009), and simple surface flux calculations with specific surface exchange coefficients (sfcmodel=1, Bryan & Rotunno, 2009). No cumulus convection scheme is used, and a Newtonian relaxation term is included in the thermodynamic equation to mimic longwave radiative cooling (rterm=1, Rotunno & Emanuel, 1987). The sea surface temperature is maintained at 31°C. An f-plane with the Coriolis parameter of 5×10^{-5} s⁻¹ is assumed, and the moist tropical sounding of Dunion (2011) is adopted. An axisymmetric vortex shaped by the tangential wind profile as in Rotunno and Emanuel (1987) is used to initialize the model. The initial TC vortex size is 1000 km in radius and extends from the surface to a height of 20 km. The maximum wind speed is 15 m s⁻¹. To find out the dominant mechanism that results in the variation of the ERC timescale, two vortices with distinct CE duration are simulated. The one (RMW110) whose CE structure lasts for 7 h has an initial radius of maximum wind (RMW) of 110 km, while the other (RMW180) that produces a 17-hour long ERC event is given an initial RMW of 180 km.

3. Results from OM3L simulation

3.1 Boundary layer dynamics

Figure 2 shows the plane view of total wind speeds for experiments R80, R100 and R120 with the smallest, median and the largest moat width, respectively. There are two radially separated extrema of total wind speeds indicative of the inner and outer eyewall, respectively, until the ERC

completes in each experiment. While the inner eyewalls are of the same strength by experimental design, the discrepancy in moat width results in different intensities of the outer eyewalls (Figures 1 and 2), which hardly affects the inner eyewall decay in terms of the boundary layer dynamics and will be discussed shortly. Generally, the evolution of concentric eyewalls in OM3L experiments is axisymmetric throughout most time of simulations, except for the later stage in experiments R100 (Figure 2h), R110 (not shown) and R120 (Figure 2l) in which barotropic instability emerges at the time around 42 h. The instability causes inward mixing of low potential vorticity (not shown) and is reflected by the rapid decrease of wind speed near the inner eyewall (Figures 3a and 3d). Although the excitation of the instability is assumed to be an effective pathway to terminate an ERC (Kossin et al., 2000; Lai et al., 2019; Lai, Hendricks, & Yau, 2021; Lai, Hendricks, Yau, & Menelaou, 2021), its occurrence is somewhat random. The vortex Rossby waves can not explain the decreasing trend in tangential winds in the inner eyewalls in R100, R110 and R120 before the instabilities show up and in R80 and R90 in which no instability occurs. For this reason, this study will not discuss the role of wave instability and will instead focus on the axisymmetric dynamics. Note that this does not imply that wave instability or other asymmetric dynamics are insignificant. For example, Tsujino et al. (2017) found that the generation of negative potential vorticity due to the asymmetric eyewall structure could prevent eyewall contraction and elongate the concentric eyewall duration. Though asymmetric structure is a common feature of real TCs, we believe that an examination from the axisymmetric perspective is the first step towards a more comprehensive understanding of ERC.

254

255

256

257

258

259

260

261

262

263

264

265

266

267

268

269

270

271

272

273

274

275

276

277

278

279

280

281

In the OM3L model, we define the eyewall intensity as the maximum tangential wind speed in the boundary layer because a wind extremum in the lower free atmosphere does not always show up near the outer eyewall even with a strong boundary layer updraft. The moat width is defined as the radial extent of the downdraft region between the inner and outer eyewalls (the radial distance between the circular and square points in Figure 4). The CE duration or the ERC timescale is measured by how long the boundary layer wind extrema of both the inner and outer eyewalls coexist. It is evident that the inner eyewall in the TC with a narrower moat tends to fade away more quickly (Figure 3a). Note that although R80 is designed to have the same inner eyewall intensity

with other experiments initially, the maximum wind speed near the inner eyewall in R80 becomes the weakest during the ERC. As a result, R80 has the shortest CE duration of 27 hours while the CE structure in R120 maintains for more than 42 hours (Figure 3a).

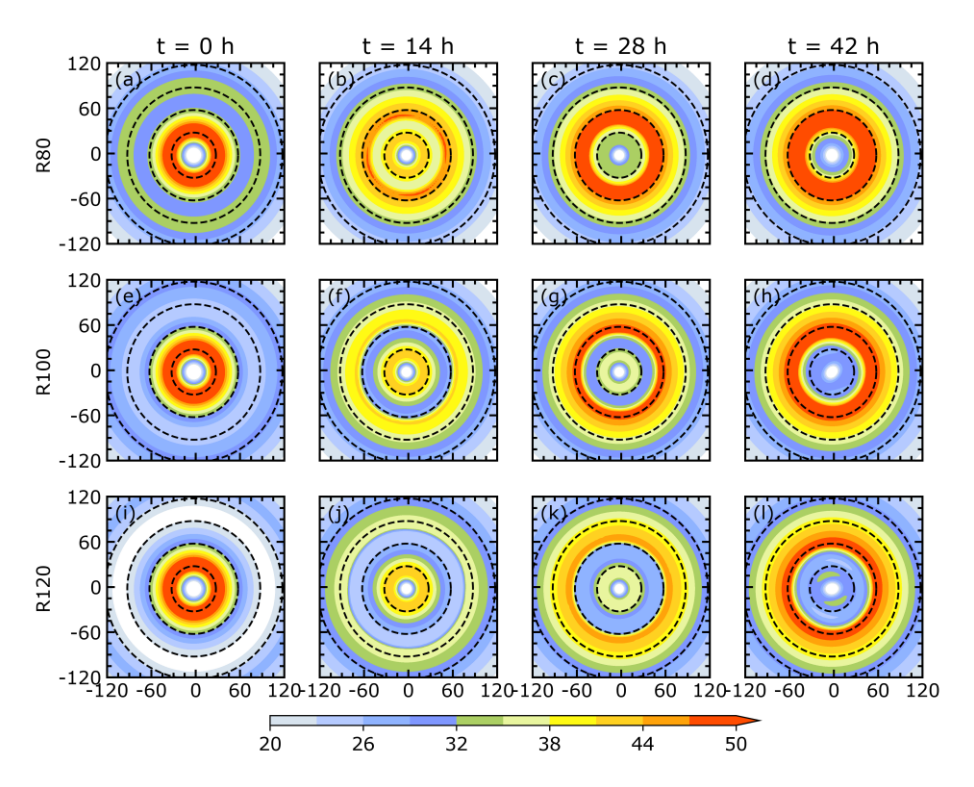


Figure 2. Plane view of total wind speeds (shading, units: m s⁻¹) in the boundary layer for experiments R80 (the first row), R100 (the second row) and R120 (the third row) at times of 0 h (the first column), 14 h (the second column), 28 h (the third column) and 42 h (the fourth column). Dashed circles in each panel show the radii of 30, 60, 90 and 120 km from the storm center, respectively.

The moat width decreases along with the inward contraction of both eyewalls except for the period of 6–12 h during which the model spin-up interferes with the inner eyewall. TCs initially with larger outer eyewalls show wider moats throughout the simulations (Figures 3b and 3c). Considering the fact that the ERC timescale is closely tied to the decay rate of the inner eyewall, we concentrate on its intensity tendency. Figure 3d shows the hourly maximum wind tendency of the inner eyewall in all experiments. The TC in R80 exhibits the most rapid weakening among the five experiments, except for the initial 6-12 h adjustment period.

The tangential wind budget is conducted to understand the mechanism that makes the collapse of the inner eyewall. The budget equation is written as (Xu & Wang, 2010a)

299
$$\frac{\partial \bar{v}_{b}}{\partial t} = -\bar{u}_{b} (\bar{\xi}_{b} + f_{c}) + \bar{F}_{r,b} - \bar{w}_{b} \frac{\partial \bar{v}_{b}}{\partial z} + \text{eddy}, \tag{2}$$

where u_b , v_b , w_b are the radial, tangential, and vertical velocity in the boundary layer, respectively, ξ_b is the boundary layer relative vorticity, f_c is the Coriolis parameter, $F_{r,b}$ is the diffusion and friction term in the boundary layer, and variables with an overbar represent the azimuthally average. Because the OM3L model employs a slab boundary layer without vertical mixing and the lower free atmosphere momentum cannot be advected into the boundary layer in the eyewall dominated by updraft, therefore, the contribution of vertical advection to the boundary layer tangential wind tendency at the inner eyewall is neglected. The eddy term is one order of magnitude smaller than the other terms in this case (not shown), and thus we focus on the first two terms on the left-hand side of Eq. (2).

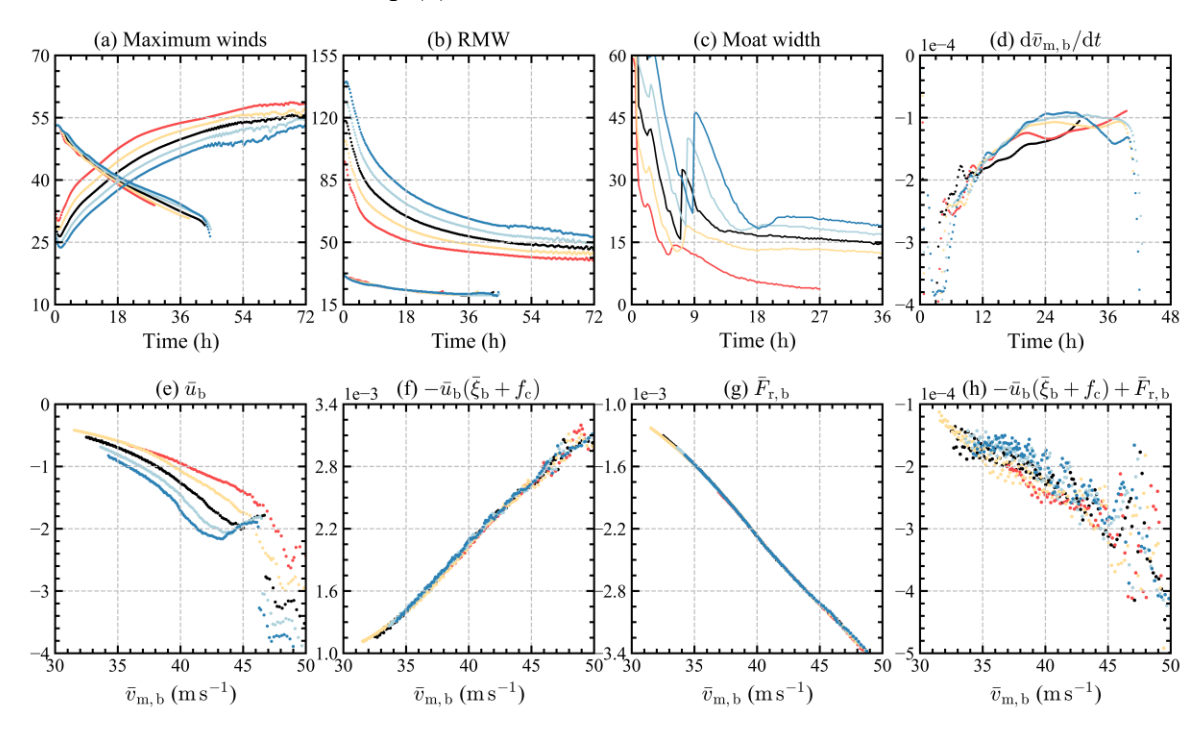


Figure 3. Temporal evolutions of (a) boundary layer maximum tangential wind speeds near the inner and outer eyewalls (units: $m \, s^{-1}$), (b) radius of boundary layer maximum tangential winds (RMW) near the inner and outer eyewalls (units: km), (c) moat width (units: km), and (d) hourly tendency of maximum boundary layer tangential wind near the inner eyewall (units: $m \, s^{-1} \, h^{-1}$) in experiments R80 (red), R90 (yellow), R100 (black), R110 (light blue), and R120 (deep blue). The areal mean within 5-km radius of the RMW of the inner eyewall of (e) boundary layer radial velocity (units: $m \, s^{-1}$), (f) the first term, (g) the second term—and (h) the sum of the first two terms—on the right-hand side of Eq. (2) (units: $m \, s^{-2}$), with respect to the maximum boundary layer tangential wind speed near the inner eyewall ($\bar{\nu}_{m,b}$).

Figure 3e shows the radial wind speed averaged within the 5-km radius of the inner eyewall in each experiment against the maximum azimuthally averaged wind speed of the inner eyewall $(\bar{\nu}_{m,b})$. Because the RMWs of the inner eyewalls are identical in all sensitivity experiments (Figure 3b), the maximum wind speeds can reasonably represent the relative intensities of eyewalls in the five TCs. TCs with larger moat widths (such as R110, R120) are likely to have stronger boundary layer inflow under the same inner eyewall intensity. According to Eq. (2), greater inflow will transport more angular momentum into the inner core and can largely compensate the negative effect of total diffusion on the boundary layer tangential wind (Figures 3f-h). Thus, the difference in the inner eyewall decay rate among all experiments is primarily resulted from the different radial velocity of air near the inner eyewall.

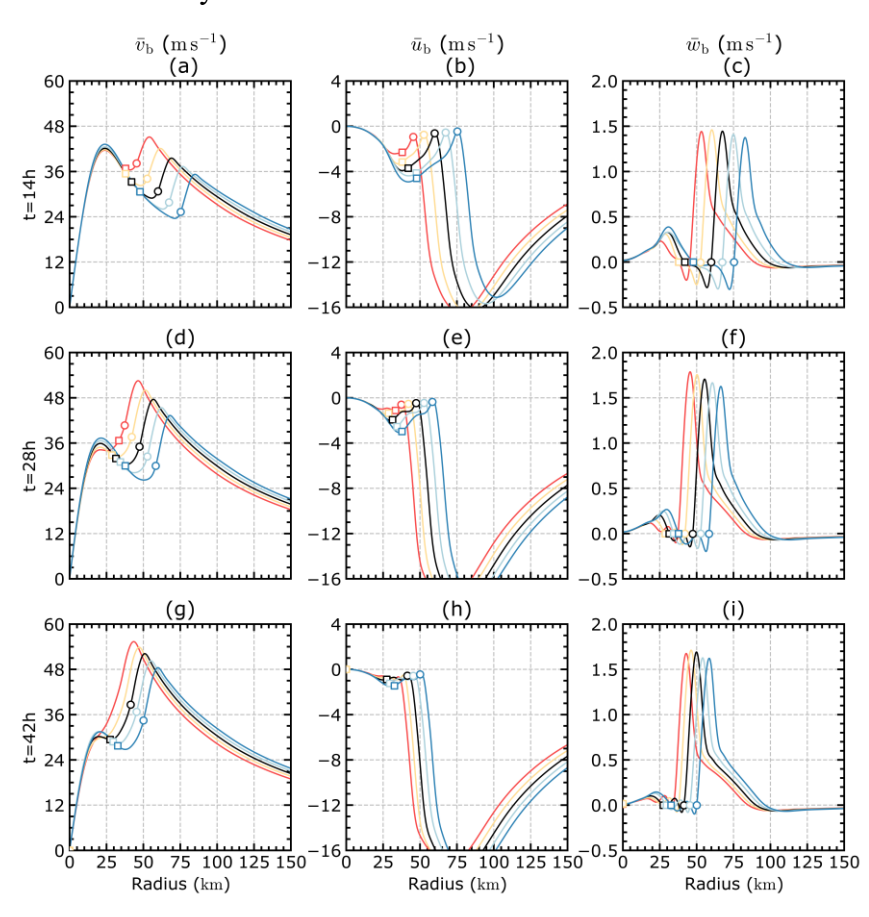


Figure 4. Radial profiles of azimuthally averaged tangential velocity (units: m s⁻¹; the first column), radial velocity (units: m s⁻¹; the second column) in the boundary layer, and vertical velocity (units: m s⁻¹; the third column) at the top of the boundary layer at the time of 14 h (the first row), 28 h (the second row), and 42 h (the third row) for experiments R80 (red), R90 (yellow), R100 (black), R110 (light blue), and R120 (deep blue). Circles and squares denote the outermost and innermost radius of the moat, respectively.

Tsujino et al. (2017) found that air masses reaching the outer edge of the inner eyewall in the boundary layer mainly come from three pathways (excluding high-frequency wandering) and air parcels travelling a long distance radially inward (the first path) account for the largest number based on the backward trajectory analysis. This result implies that the radial velocity of air parcels at the inner eyewall is determined by the velocity change along the way of the first path. Radial profiles of boundary layer inflows at the time of 14, 28, 42 h in the five experiments are depicted in the second column of Figure 4. Note that the radial profiles at early model spin-up periods are not shown for clarity. Generally, the inflow is accelerated inward in the far field at first then is significantly reduced nearly to zero by the outer eyewall. Although the degree of reduction is proportional to the outer eyewall intensity, the radial velocity of air just inside the outer eyewall seems to be identical in the five TCs. After passing through the outer eyewall air parcels are pushed inward by the pressure gradient force in the moat region, and the velocity increment should be determined by both the amplitude of the centripetal force and the acceleration distance. Considering the intrinsic limitations of the OM3L model in reproducing surface and boundary layer processes and nonlinear dynamics (Fei & Wang, 2021; Kepert, 2010a,b), we will give a more detailed analysis of the inflow budget across the moat in the full-physics model CM1 simulations in section 4.

Striking differences in the maximum boundary layer radial velocity among experiments can occur even when all TCs are of similar strengths (Figures 4a and 4b). Because the moat is much narrower in R80 than R120, air parcels in the boundary layer have less time to accelerate across the moat in the former than in the latter, consistent with Kuo et al. (2022). Therefore, R80 has the weakest inflow at the inner edge of the moat and the fastest weakening by surface friction and diffusion (Figures 3f and 3h). From then on, the disparity of weakening tendencies among the five TCs becomes increasingly distinct (Figure 3d), partly due to different moat widths and partly due to the growing discrepancy of inner eyewall intensity (Figures 4a, 4d and 4g). Besides, the stronger friction-induced boundary layer updrafts resulting from the steeper radial gradient of inflow (Figures 4c, 4f and 4i) can help maintain the wind strength in the lower free atmosphere by transporting relatively larger diabatic mass into the upper free atmosphere (Schecter & Dunkerton, 2009), which results in a stronger upper divergence so that the lower free atmosphere air pressure is kept low. Therefore, the wind fields in the boundary layer and the lower free atmosphere could evolve in a synergistic way. The importance of the friction-induced updraft and its positive feedback with the eyewall convection has also been argued in previous studies (Kepert, 2013, 2017;

3.2 Quantification of the relationship between inner eyewall weakening rate and moat width

A dataset of five hundreds idealized TCs is constructed by varying structural parameters of CEs (see section 2.1) to testify and quantify the relationship between the inner eyewall decay rate and moat width. Definitions of moat width and inner eyewall decay rate are the same as in Figure 3. The model output between the period 16–30 h of the simulation is used in the correlation calculation because the period 0–16 h is impacted by the early vortex spin-up and convective adjustment processes. The simulation after 30 hours is ignored owing to the likely excitation of barotropic instability.

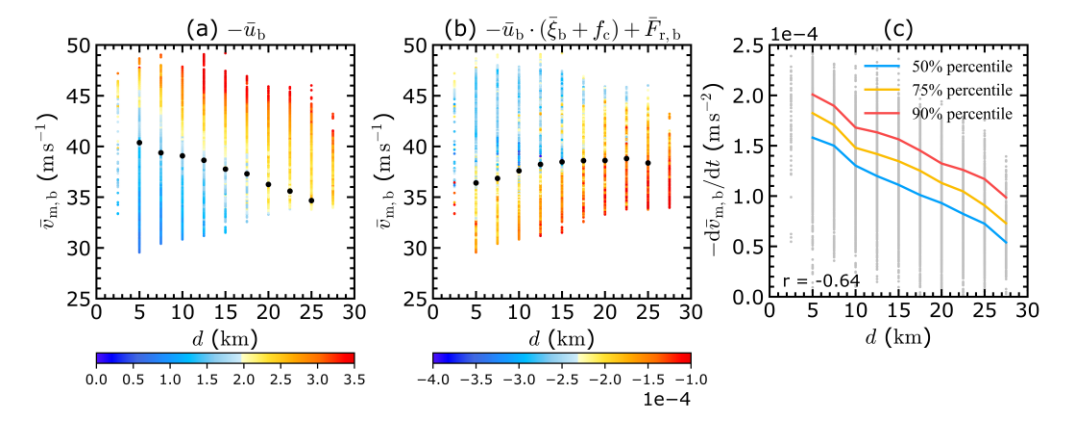


Figure 5. Scatter diagrams (color dots) of averaged (a) $-\bar{u}_b$ (units: m s⁻¹) and (b) $-\bar{u}_b(\bar{\xi}_b + f_c) + \bar{F}_{r,b}$ (units: m s⁻²) within 5-km radius of the RMW of the inner eyewall, with respect to $\bar{v}_{m,b}$ and moat width (d). Dot color varies from blue to red when the value increases. Black dots in (a) and (b) denote the average $\bar{v}_{m,b}$ at each moat width when $-\bar{u}_b$ reaches 2 ± 0.1 m s⁻¹ and $(-\bar{u}_b(\bar{\xi}_b + f_c) + \bar{F}_{r,b})$ reaches -1.5e-4 \pm 0.1e-4 m s⁻², respectively. And (c) scatter diagram of the inner eyewall decay rate $(-d\bar{v}_{m,b}/dt)$ versus moat width. The blue, yellow and red line represents the 50%, 75% and 90% percentile, respectively. The correlation coefficient is -0.64, which is statistically significant over 99% confidence level.

It is shown in Figure 5a that both the eyewall intensity and the moat width can modify the radial velocity at the inner eyewall. Specifically, black dots in the figure denote the averaged $\bar{v}_{\rm m,b}$ when inflow reaches $2\pm0.1~{\rm m~s^{-1}}$ at each moat width. The decreasing trend of these dots with the moat width indicates that the inflow at the inner eyewall can reach $2~{\rm m~s^{-1}}$ with a weaker eyewall and wider moat, implying the moat width is positively correlated with the inflow intensity. Similarly, the increasing trend of black dots in Figure 5b, which represent the averaged $\bar{v}_{\rm m,b}$ when the sum of the first two terms on the right-hand side of Eq. (2) $(-\bar{u}_{\rm b}(\bar{\xi}_{\rm b}+f_{\rm c})+\bar{F}_{\rm r,b})$ reaches

 $(-1.5 \pm 0.1) \times 10^{-4} \,$ m s⁻² at each moat width. This means that the radial flux of absolute vorticity is larger with a wider moat and inner eyewalls are more likely to persist against surface friction. In general, these statistics deduced from the idealized TC dataset consolidate the analysis of the five sensitivity experiments discussed in the previous section.

Correspondingly, the inner eyewall decay rate shows a remarkable decreasing trend as the moat width increases. The correlation coefficient between the two parameters reaches -0.64, which is statistically significant at 99% confidence level (Figure 5c). This corroborates the observational fact that the CE duration is positively correlated to the moat width, as the inner eyewall decay rate is directly related to the maintenance of CE structure. According to the results from the OM3L model, which employs simplified thermodynamic processes, there are little differences in thermodynamic fields among the five experiments (not shown). We suggest that the boundary layer dynamics are essential to the ERC and its timescale, which will be further clarified based on results from the full-physics model CM1 in the next section.

4. Results from CM1 simulations

4.1 Boundary layer dynamics

Although the OM3L model provides some insights into the ERC dynamics, it has some limitations in simulating authentic TC structures and the associated thermodynamics. Therefore, the full-physics cloud model, CM1 (Bryan & Rotunno, 2009), is used to further examine the key processes leading to the inner eyewall decay by contrasting two experiments (RMW110 and RMW180) in which TCs behave quite differently in terms of the timing and evolution during the ERCs. Figures 6 and 7 show the azimuthally averaged 10-m-height tangential wind speeds and composite radar reflectivity in RMW110 and RMW180, respectively. Both TCs experience ERC more than once (not shown), have similar inner eyewall strengths but with the distinct moat width when the last ERC begins. Thus, the last ERC event during the simulation period in each TC is chosen for a detailed analysis. The outer eyewall forms at 153 h of the simulation and the inner eyewall vanishes at 160 h in RMW110, while the last ERC event starts at 183 h and ends at 200 h in RMW180. The duration of the CE structure is 10 hours longer in RMW180 than in RMW110 (Figures 6a and 7a). When the secondary eyewalls form (one hour before the inner eyewalls disappear), the inner eyewalls in the two TCs exhibit similar intensities with maximum tangential winds of about 57 (44.5) m s⁻¹ and RMWs of about 30 (36) km, respectively. These two

experiments portray the impact of outer eyewall radius on ERC evolution with different outer eyewall structures. The RMW of the outer eyewall in RMW110 at the time of the SEF is 90 km and contracts inward by 25 km in 7 hours, while in RMW180 the outer eyewall shifts from 128 km to 101 km in 17 hours, which is 2 km h⁻¹ slower than that in RMW110. The larger radial location of the SEF and smaller contraction rate in RMW180 lead to a weaker eyewall when the ERC completes. In terms of the inner eyewall intensity change, RMW110 has a larger decay rate after the SEF, with a maximum exceeding 15 m s⁻¹ h⁻¹ (Figure 6b), while the inner eyewall in RMW180 decays at a much slower rate especially during the early stage of the ERC (Figure 7b). Moreover, the moat, which is defined as the low-echo or echo-free region between the inner and eyewall eyewalls is much clearer and wider in RMW180 owing to its distant outer eyewall. In general, the initial structures of concentric eyewalls in OM3L and CM1 models are similar, indicating that the prescribed TC structures in OM3L experiments are reasonable. Although the inner eyewalls weaken at slower rates and persist longer due to the minimal parameterizations of cumulus convection and the slab boundary layer in OM3L simulations, the overall structures and evolutions of concentric eyewalls are comparable in the two model experiments.

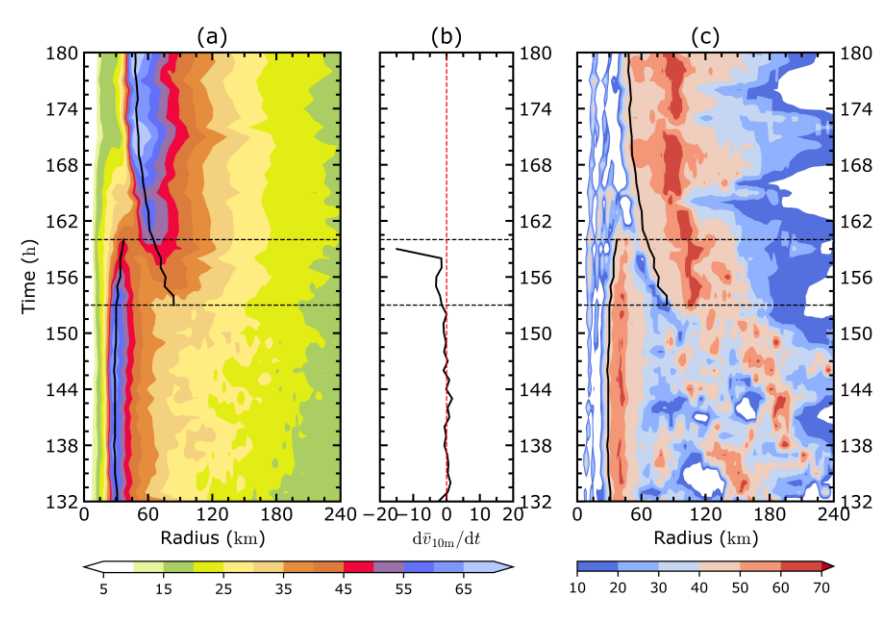


Figure 6. Time-radius Hovmöller diagrams of the azimuthally averaged (a) 10-m-height tangential wind (units: m s⁻¹), (b) temporal profile of hourly tendency of maximum 10-m-height tangential wind near the inner eyewall (units: m s⁻¹ h⁻¹), and (c) composite radar reflectivity (units: dBZ) for experiment RMW110. Black solid contours in (a) and (c) denote the RMWs of the inner and outer eyewall, respectively. The black horizontal dashed lines indicate the starting and ending of the ERC, respectively.

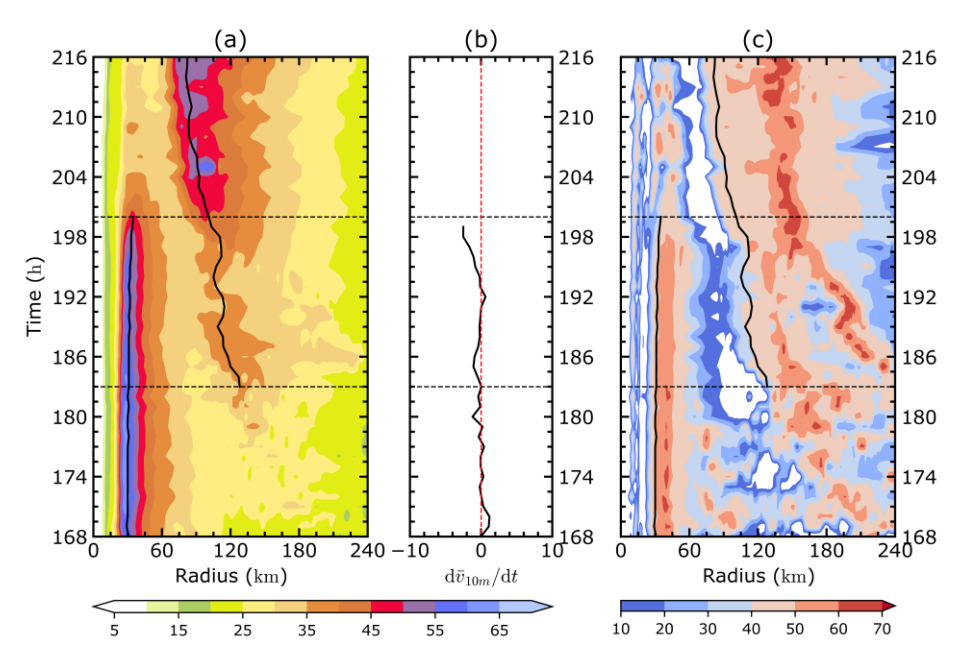


Figure 7. The same as Figure 6 but for experiment RMW180.

Although both an uncoupled slab boundary model (Kuo et al., 2022) and a coupled Ooyamatype model are utilized to analyze how the inflow is invigorated within the moat and how it influences the evolution of the inner eyewall, it is still unclear whether the mechanism takes effect and is important in the full-physics model simulations. Therefore, the radial wind budget is conducted to elucidate the boundary layer dynamics. Under the assumption of a quasi-steady state approximation (i.e. the local derivative of the radial wind $\partial u/\partial t$ is negligible), Wang et al. (2013) gave the depth-averaged form of the inflow diagnostic equation as (neglecting the eddy terms)

$$\frac{1}{r}\frac{\partial r\bar{u}_{b}^{2}}{\partial r} = \underbrace{-\frac{1}{H}\int_{0}^{H}\frac{1}{\bar{\rho}}\frac{\partial\bar{p}}{\partial r}dz}_{PGF} + \underbrace{\frac{1}{H}\int_{0}^{H}\frac{\bar{v}^{2}}{r}dz}_{CNF} + \underbrace{\frac{1}{H}\int_{0}^{H}\bar{F}_{r}dz}_{FRF} - \underbrace{\frac{\bar{w}\bar{u}}{H}|_{z=H}}_{UWT},$$
(3)

where u, v, ϕ are radial, tangential wind speeds and geopotential height, respectively; r is the radius; f_c is the Coriolis parameter; H is the boundary layer height; terms with subscript b are the depth averages from the surface to the top of the boundary layer $(\bar{u}_b^2 = \frac{1}{H} \int_0^H \bar{u}^2 dz, \bar{v}_b = \frac{1}{H} \int_0^H \bar{v} dz)$; PGF, CNF, CF, FRF represent pressure gradient, centrifugal, Coriolis and friction forces, respectively, and UWT is related to the momentum flux at the top of the boundary layer. The sum of the first three terms on the right hand of Eq. (3) is often called the agradient force (AGF) and the sum of all forces is the net radial force (NRF). By integrating Eq. (3) along the radial direction, one can obtain

$$r\overline{u}_{b}^{2} - R\overline{U}_{b}^{2} = \int_{R}^{r} r' \times NRF \, dr'. \tag{4}$$

where R, \overline{U}_{b} is the radius and radial wind speed in the distant. From the Lagrangian point of view, Eq. (4) can be rendered that the radial kinematic energy gained by air molecules equals to the work imposed by the net radial force.

Figure 8 shows the diagnosed and actual hourly averaged $\bar{u}_{\rm b}$ distributions in RMW110 and RMW180 during the ERC, using the model output at every 6 minutes with the boundary layer height of 571 m. The height of 571 m is chosen so that the layer below which is dominated by inflow throughout the ERC period when the boundary layer height near the inner eyewall is decreasing. Besides, the result is not sensitive to the choice of the boundary layer height (not shown). Since we focus on the re-acceleration process within the moat, only radial winds in the moat region are reproduced based on Eq. (4) for simplicity. In this case, R is the outermost radius of the moat, \overline{U}_b is the depth-integrated, azimuthally averaged radial wind speed at the radius R. It is shown that the diagnosed radial wind is almost identical to that in the simulation, implying that the assumption of pseudo-stationary boundary layer is reasonable. As indicated by Wang et al. (2013), the pressure gradient and centrifugal forces are the greatest and largely compensate each other. Together with the Coriolis force, they constitute the AGF that can accelerate the boundary layer flow toward the inner eyewall. The FRF term always encumbers air motion, and the UWT term has a nonnegligible contribution in the eyewalls but is negligible in the moat region. Positive NRF is mainly confined to the ascending region and its magnitude can reflect the eyewall intensity. Negative NRF is most prominent in the moat region, suggesting a re-intensification of the inflow.

According to Eq. (4), the radial velocity of the air parcels reaching the inner eyewall is determined by the velocity before the acceleration (i.e., \overline{U}_b), the moat width (R-r) and the NRF. Shortly after the SEF, both TCs have comparable radial velocities after passing through the outer eyewall and similar maximum NRF within the moats, but there is greater inflow at the inner eyewall in RMW180 (Figures 8a and 8e). This is because the wider moat in RMW180 provides air to travel longer distance to accelerate, leading to a larger speed increment as indicated by the black arrows in the Figure 8. Specifically, the increase of radial velocity within the moat in RMW180 is 5 m s⁻¹ greater than that in RMW110, just the same as the excessive amount of the inflow at the inner eyewall.

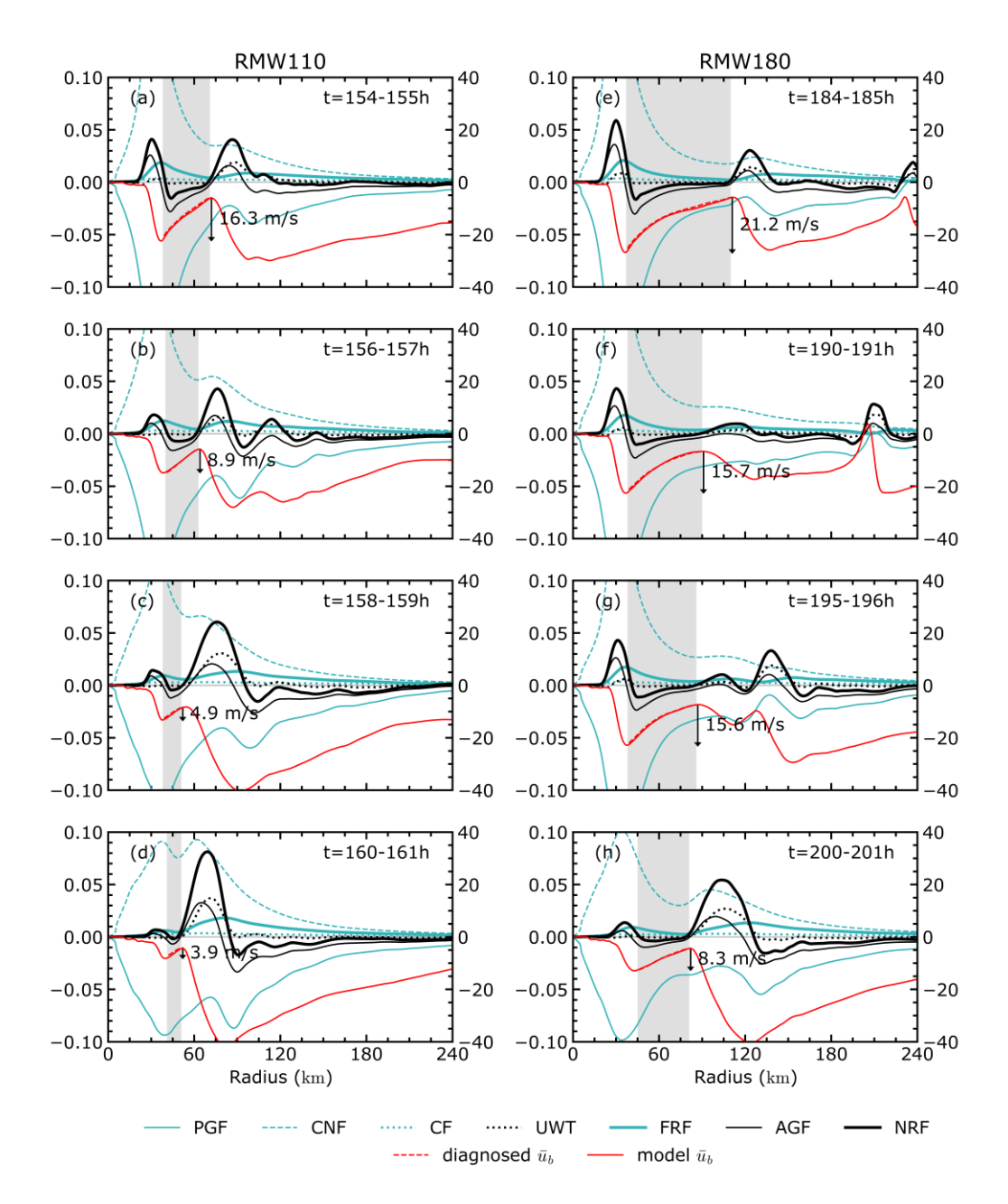


Figure 8. (a) Radial profiles of hourly (using 6-min-intervel model output) and vertically (from the lowest model level to the height of 571 m) averaged pressure gradient force (PGF), centrifugal force (CNF), Coriolis force (CF), friction force (FRF), the agradient force (AGF=PGF+CNF+CF), vertical flux of radial momentum at the boundary layer top (UWT), and the sum of all of these terms (NRF), corresponding to the left y-axis. The unit of force is 10⁻³ N kg⁻¹. Solid and dashed red lines are hourly and vertically averaged radial velocity (units: m s⁻¹) from the model output and reconstructed based on Eq. (4), respectively, corresponding to the right y-axis. The gray shadings indicate the moat region. Black arrows and numbers alongside point out the velocity increments across the moat region. Results for both RMW110 (left column) and RMW180 (right column) are shown at different times.

Consistent with the results discussed in the section 3, the radial velocity on the inner side of the outer eyewall does not change obviously with the outer eyewall strength, though the increased amount of radial velocity is reduced due to the developing outer eyewall (Figure 8). However, due to the larger weakening tendency of the inner eyewall since the SEF and then the faster contraction of the outer eyewall in RMW110, both the NRF and the moat width are relatively small compared to those in RMW180 during the later stage of the ERC (Figures 8b-d and 8f-h). Thus, based on Eq. (4) the radial velocity at the inner eyewall is smaller throughout the ERC in RMW110. Besides, the intensification of the outer convection resulted from the eyewall contraction will lower the surface pressure, which can reduce the horizontal pressure gradient across the inner eyewall through the hydrostatic adjustment (Wang, 2009). This further reduces the kinematic energy gained by the air parcels when they are pushed inward by weaker AGF.

According to the tangential wind tendency equation Eq. (2), an inner eyewall of the same intensity but supported by greater inflow is more capable of offsetting the decreasing tendency induced by the surface friction, diffusion, and vertical advection. Since the RMWs of the inner eyewalls in both TCs are very similar (Figures 6a and 7a), the maximum wind speeds can be rendered proportional to the eyewall intensity. Figure 9a shows the boundary layer radial velocities in RMW110 and RMW180, each of which is vertically averaged from the surface to the boundary layer top (571 m) and is horizontally averaged within 5-km radius of the RMW of the inner eyewall, with respect to the maximum wind speed at 10-m height near the inner eyewall $(\bar{v}_{m,h})$. Consistent with the result of OM3L experiments, the radial velocity decreases along with the dropping intensity of the inner eyewall, which gradually loses the ability to accelerate inflow. Stronger inflow can be achieved under the same inner eyewall intensity in a TC with a wider moat especially during the early stage of the ERC, since the moat width would be remarkably reduced because of the eyewall contraction afterwards. Therefore, there is greater radial inward flux of absolute vorticity in the inner-core region in RMW180 (Figure 9b). With respect to $\bar{v}_{\rm m,b}$, values of $\bar{F}_{\rm r,b}$ in both experiments are similar, but there is larger negative contribution from the vertical advection to boundary layer tangential winds in RMW180, due to the stronger eyewall updraft (Figure 9c). However, as indicated in Figure 9d, the positive contribution from the radial flux of absolute vorticity can nearly balance the negative tendency due to vertical advection and $\bar{F}_{r,b}$ when the moat width is sufficiently large, like during the first few hours of the ERC in RMW180. On the contrary, the radial flux of absolute vorticity term hardly overcomes other negative terms in RMW110, resulting in a rapid inner eyewall weakening. Thereby, it has been justified in both simple and full-physics models that the moat width can significantly modulate the inner eyewall decay rate.

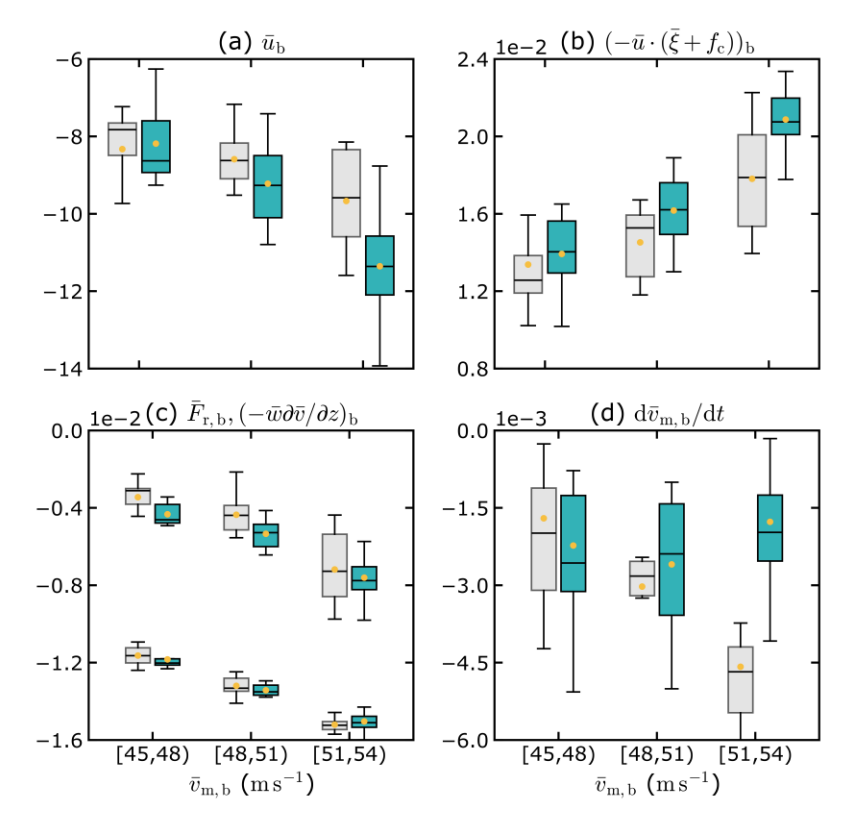


Figure 9. Box plots for the depth-averaged (from the lowest model level to the height of 571 m) and areal mean (within the 5-km radius of the RMW of the inner eyewall) (a) radial velocity (units: m s⁻¹), (b) radial flux of absolute vorticity (units: m s⁻²), (c) friction and diffusion (at the lower part of the panel, units: m s⁻²) as well as vertical advection of tangential wind (at the upper part of the panel, units: m s⁻²), and (d) local tangential wind tendency (units: m s⁻²), grouped by the maximum 10-m-height wind speed near the inner eyewall. The box indicates the range from the 25th to 75th percentiles of the distributions, with a black line at the median as well as a yellow dot showing the mean, and the whiskers indicate the range of the distributions. Results of RMW110 and RMW180 are denoted by gray and cyan box, respectively.

4.2 Boundary layer thermodynamics

Although the boundary layer dynamics are emphasized above, previous studies suggested that thermodynamic processes can influence the concentric eyewall duration as well. Zhou and Wang (2011) argued that sharp gradient of θ_e and enhanced cold advection near the inner eyewall would expedite the demise of the eyewall when the moat was narrow, which may imply that the moat

width can modulate the ERC timescale with the help of boundary layer thermodynamics in addition to the dynamical mechanism. Nevertheless, Tsujino et al. (2017) found the net θ_e flux into the inner eyewall remained positive (though getting less after the SEF) during the two ERC events of Typhoon Bolaven (2012). We also notice that θ_e in the boundary layer and the lower troposphere has been increasing during the ERC period in RMW110 & RM180 (Figure 10). The magnitude of the θ_e change solely caused by the decrease in pressure is one order smaller than the total change (not shown). Thus, there should be significant contribution from the temperature and water vapor to the increasing tendency of θ_e .

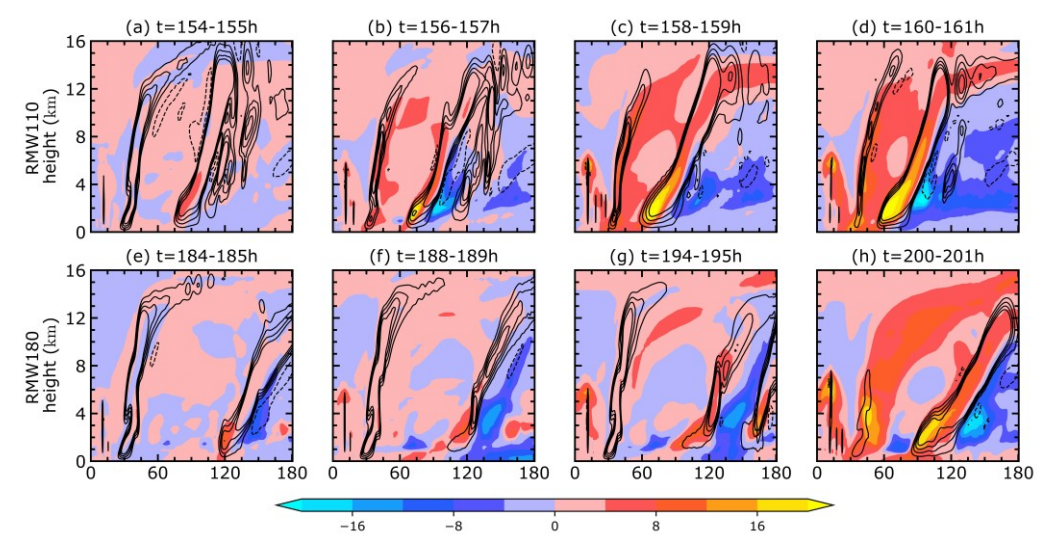


Figure 10. The hourly averaged equivalent potential temperature (θ_e , shading, units: K) anomaly at different times (a-d) in RMW110 with respect to the mean θ_e between the time of 153 to 154 h, and (e-h) in RMW180 with respect to the mean θ_e between the time of 183 to 184 h. Black contours represent vertical motions with contours of -0.5, 0.5, 1, 1.5, 2.0 m s⁻¹.

The equivalent potential temperature budget analysis is carried out to examine processes that have contributed to the positive θ_e tendency. Results of the two experiments are qualitatively the same, thus only the diagnosis for RMW110 is shown here. θ_e is defined as a function of potential temperature θ and mixing ratio of water vapor q_v

$$\theta_e = \theta + \frac{L_v q_v}{C_p \pi},\tag{5}$$

where L_v , C_p , and π are latent heat, specific heat at constant pressure and Exner function, respectively. Here, we have $L_v = 2.5 \times 10^6 \, \text{J} \cdot \text{kg}^{-1}$ and $C_p = 1004.0 \, \text{J} \cdot \text{kg}^{-1} \cdot \text{K}^{-1}$, which are

used in the CM1 model. By taking the time derivative of each term on the right-hand side of the Eq. (5), the θ_e tendency equation is written as (see the appendix in Zhou & Wang, 2011)

567
$$\frac{\partial \theta_{e}}{\partial t} = -\frac{\partial u\theta}{\partial r} - \frac{\partial w\theta}{\partial z} + F_{\text{turb},\theta} + F_{\text{diff},\theta} + F_{\text{db},\theta}$$

$$-\frac{L_{v}}{C_{p}\pi} \left(\frac{\partial uq_{v}}{\partial r} + \frac{\partial wq_{v}}{\partial z} \right) + F_{\text{turb},q_{v}} + F_{\text{diff},q_{v}} + F_{\text{db},q_{v}}. \tag{6}$$

Both θ and q_v tendencies consist of horizontal advection (HADV), vertical advection (VADV), turbulence (TURB), diffusion (DIFF), and contribution from diabatic processes (DB) such as cloud microphysics and radiation. In the moist adiabatic process θ_e is conserved $(F_{\mathrm{db},\theta} + F_{\mathrm{db},q_v} = 0)$. Although moist processes are not strictly reversible in real TCs, $F_{db,\theta}$ and F_{db,q_v} still largely offset each other. Figure 11 shows the contribution from each component averaged between 158– 161 h when the inner eyewall undergoes pronounced weakening. Consistent with the work of Zhou and Wang (2011), there is significant horizontal advection of low θ_e from the moat to the innercore region in the boundary layer (Figures 11a and 11f). However, vertical turbulent mixing of high potential temperature from the sea surface significantly increases the θ in the boundary layer (Figure 11d), and the moisture is greatly enriched by both vertical advection and vertical turbulence mixing (Figures 11g and 11i). Although the sea surface temperature remained constant throughout the simulation, it is suggested that enthalpy reduction induced by low- θ_e air in the boundary layer can be greatly recovered as long as there is enough local supply of heat and moisture (Figures 11ko). As a result, the moist entropy increases and the thermodynamic condition in the boundary layer is favorable for the inner eyewall to sustain during the ERC. Based on the θ_e budget, we suspect that the boundary layer thermodynamics is not essential to the inner eyewall decay, which has been reported before by Tsujino et al. (2017), indicating that the result may not be an exceptional phenomenon.

4.3 The outer eyewall contraction

565

566

569

570

571

572

573

574

575

576

577

578

579

580

581

582

583

584

585

586

587

588

589

590

591

592

593

It has been clarified that the moat width is an important ingredient that can influence the inner eyewall decay rate, hence a more comprehensive understanding on the eyewall contraction is beneficial to predicting the ERC timescale. The eyewall contraction in a single-eyewall TC has been extensively studied (Li et al., 2019; Li et al., 2021; Shapiro & Willoughby, 1982; Wang, 2008, 2009; Xu & Wang, 2010a, 2010b). Generally, it is believed that diabatic heating in the eyewall induces greater wind tendency inside the RMW than the tendency at and outside of the current

595

597

598

599 600

601

602

594

Figure 11. The composite azimuth-mean equivalent potential temperature (θ_e) budget over the 3-h period of 158– 161 h in RMW110 (shading, units: K s⁻¹). The individual terms on the right-hand side of Eq. (6) for (a-e) potential temperature (θ) and (f-j) specific humidity (q_v). The sum of VADV, DB, TURB and DIFF terms of (k) θ and (l) q_v are also shown. Total tendency of θ , q_v and θ_e is given in panel (m), (n), (o) respectively. Black contours represent vertical motions with contours of -0.5, 0.5, 1, 1.5, 2.0 m s⁻¹.

0.0

1.2

1.8 1e-3

-0.6

Wang (2009) proposed that active outer spiral rainbands can enlarge the TC inner-core size and limit the intensity by producing a more vertically tilted eyewall in a single-eyewall TC. Such a phenomenon also happens to the outer eyewall in a double-eyewall TC as shown in the experiments of RMW110 and RMW180. This is similar to what was recently found in a numerical study by Yang (2024), who also showed the active outer spiral rainbands may slow down the outer eyewall contraction and affect the intensity change during the eyewall replacement cycle of TCs.

603

604

605

606

607

608

609

610

611

612

613

614

615

616

617

618

619

620

621

622

623

624

625

626

627

628

629

630

631

632

633

Since RMW180 has stronger winds in the outer-core region, there is more energy input from the ocean to support the development of outer spiral rainbands in the TC (Xu & Wang, 2010a). As depicted in Figure 7c, the rainband activity outside the outer eyewall becomes more active from 178 h of the simulation in RMW180, which is likely to have affected the formation of the secondary eyewall. One and a half hours after the SEF, outer spiral rainbands organize into a lively convective system but without a third wind maximum (Figure 7a). Until the ultimate merging of the rainbands into the outer eyewall at the time of 196 h, the development of outer spiral rainbands impedes and even suspends the contraction of the outer eyewall by generating local positive wind tendency and strengthening inertial stability in the outer-core region and thus preventing inflow near the outer eyewall. Besides, consistent with the finding of Wang (2009), the outer eyewall in RMW180 exhibits a more outwardly tilted vertical structure than that in RMW110 (Figure 10), which has much less active outer rainbands. The outwardly tilted eyewall convection would result in a larger wind tendency outside rather inside the RMW (Wang, 2008). We can see from Figure 12 that there is pronounced positive tangential wind tendency and large inflow inside the RMW of the outer eyewall in RMW110, while there is a substantially reduced tangential wind tendency and inflow at the inner edge of the outer eyewall and weak negative tendency outwardly adjacent to the eyewall in RMW180, especially during 185-196 h. Consequently, this results in greater negative radial gradient of tangential wind tendency and contraction rate (2.7 km h⁻¹) in the former (Stern et al., 2015). In contrast, the contraction rate of the outer eyewall is only 1.6 km h⁻¹ in the latter. After 196 h when the outer rainbands are merged into the outer eyewall, the eyewall contraction rate becomes larger due to the enhancement of inflow and tangential wind near the inner edge of the outer eyewall in RMW180 (Figure 12b). Given the generally slow outer eyewall contraction, the moat width in RMW180 remains relatively large, hence there is more momentum supply for the inner eyewall to survive. On the other hand, there is no significant difference in outer eyewall contraction rate among OM3L experiments (Figure 3b), due to the absence of outer rainband activity.

Several sensitivity experiments are conducted to confirm the impacts of outer spiral rainbands

on the contraction rate of the outer eyewall. By artificially multiplying a coefficient α to the diabatic heating/cooling rate in the region outside a radius of 120 km after 120 h of the simulations from the microphysics scheme (as done in Wang, 2009), we can alter the activity of outer rainbands. The particular time is chosen when both TCs maintain at a relatively steady intensity, and the time is long enough for the outer core adapting to the new diabatic heating rate prior to the SEF. The particular radius is selected beyond which there are clusters of convective cells in both experiments prior to the SEF (Figures 6c and 7c). For RMW110, in which the TC has relatively small ERC timescale, we explore whether active outer rainbands could elongate the concentric eyewall duration or not by reducing the diabatic cooling rate by 20% (α=0.8, RMW110-Cool080) where the diabatic heating rate is negative or by increasing the diabatic heating rate by 10% (α =1.1, RMW110-Heat110) where the diabatic heating rate is positive. On the contrary, for RMW180, we attempt to shorten its ERC timescale by increasing the diabatic cooling rate by 20% ($\alpha = 1.2$, RMW180-Cool120) or by reducing the diabatic heating rate by 10% ($\alpha = 0.9$, RMW180-Heat090) to suppress outer rainband activity. Because increasing (decreasing) diabatic cooling rate is less effective in terms of suppressing (strengthening) convection, the absolute value of the coefficient is set to be greater.

634

635

636

637

638

639

640

641

642

643

644

645

646

647

648

649

650

651

652

653

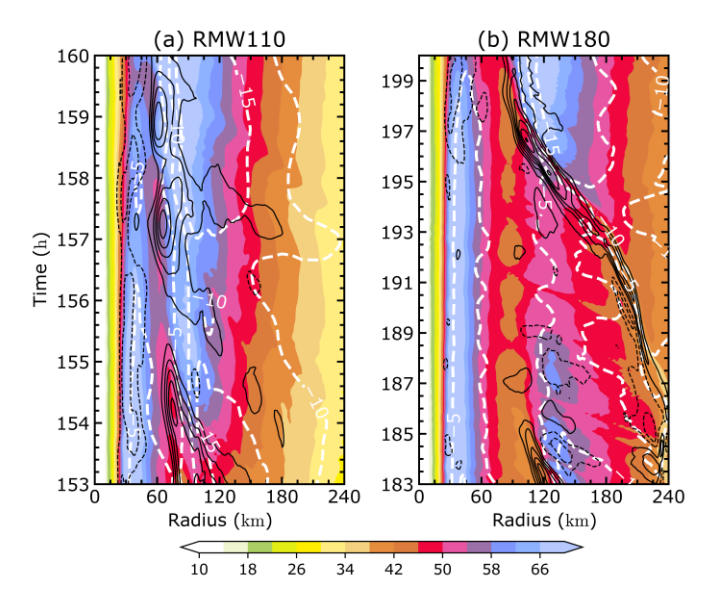


Figure 12. Time-radius Hovmöller diagrams of height-averaged tangential wind below 3 km (shading, units: m s⁻¹), its hourly tendency (black contours, units: m s⁻¹ h⁻¹) at levels from -10 to 16 m s⁻¹ h⁻¹ (except for zero level) with an interval of 2 m s⁻¹ h⁻¹, and height-averaged radial velocity below 3 km (white contours, units: m s⁻¹) at levels of -15, -10 and -5 m s⁻¹ for (a) RMW110 and (b) RMW180.

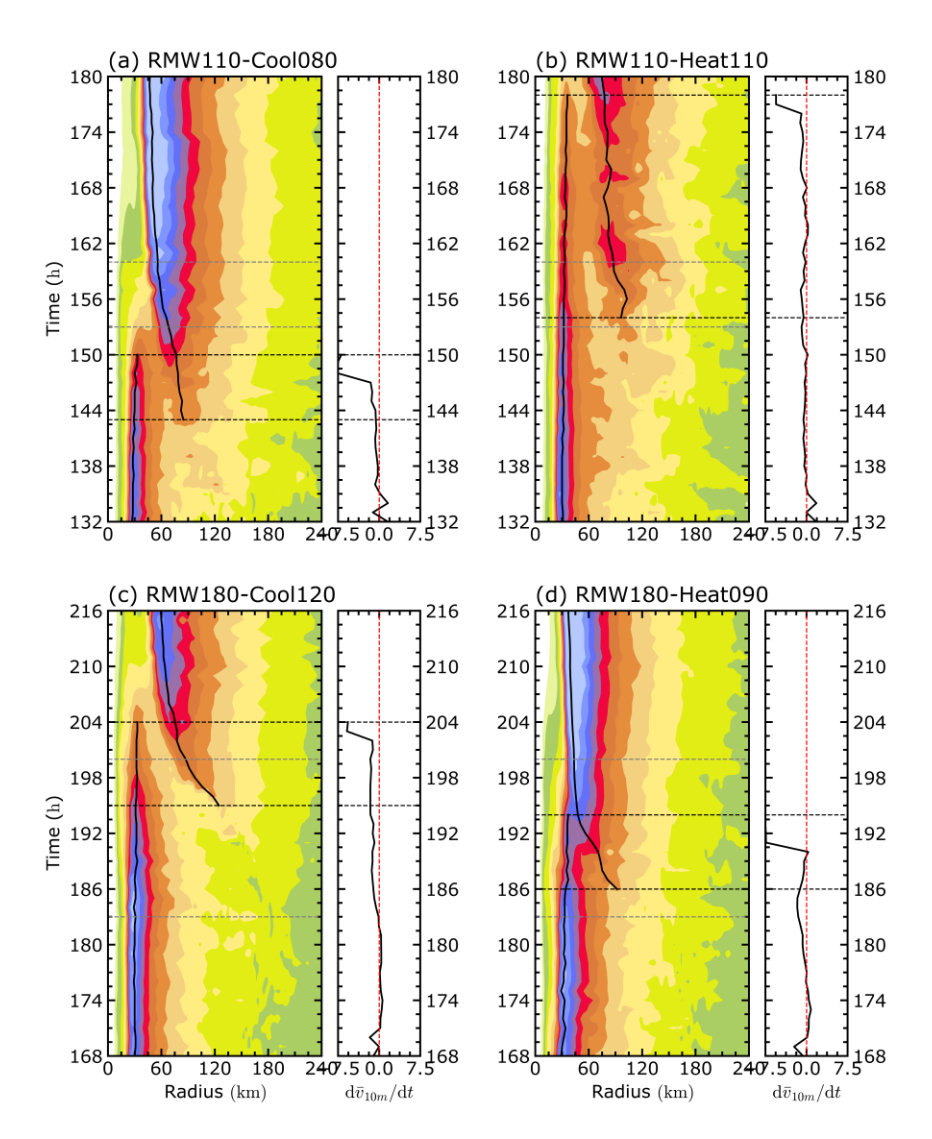


Figure 13. Time-radius Hovmöller diagrams of azimuthally averaged 10-m-height tangential wind (units: m s⁻¹) and hourly tendency of maximum 10-m-height tangential wind near the inner eyewall (units: m s⁻¹ h⁻¹) in (a) RMW110-Cool080, (b) RMW110-Heat110, (c) RMW180-Cool120, and (d) RMW180-Heat090. Black solid contours denote the RMWs of the inner and outer eyewall. Black dashed lines indicate the start and the end of the ERC event in each sensitivity experiment, and gray dashed lines in panel (a) & (b) and (c) & (d) indicate the start and the end of the ERC event in RMW110 and RMW180, respectively.

Figure 13 shows the concentric eyewall evolutions in the four sensitivity experiments. In RMW110-Cool080, decreasing the cooling rate makes the secondary eyewall form earlier but does not modify the ERC timescale much (Figure 13a), which may because reducing diabatic cooling only is less effective in enhancing rainband activity. While in RMW110-Heat110, the inner eyewall decay rate is significantly diminished, and the concentric eyewall duration is extended to 24 h in contrast to 7 h in RMW110 (Figure 13b). Although TCs in the RMW110 group have secondary

eyewalls forming all near the radius of 90 km, they present distinct temporal evolutions of the RMW of the outer eyewall. This can be seen from Figure 14a, which illustrates that the secondary eyewall in the TC with artificially enhanced convective activity in outer rainbands contracts inward at a smaller rate, especially evident in RMW110-Heat110. In the RMW180 group, the secondary eyewall shows up earlier at a smaller radius and the concentric eyewall duration is sharply curtailed by either enhancing diabatic cooling or reducing diabatic heating rate (Figures 13c and 13d). In addition, the contraction rates of the outer eyewall in both experiments are significantly accelerated compared to that in RMW180 (Figure 14b).

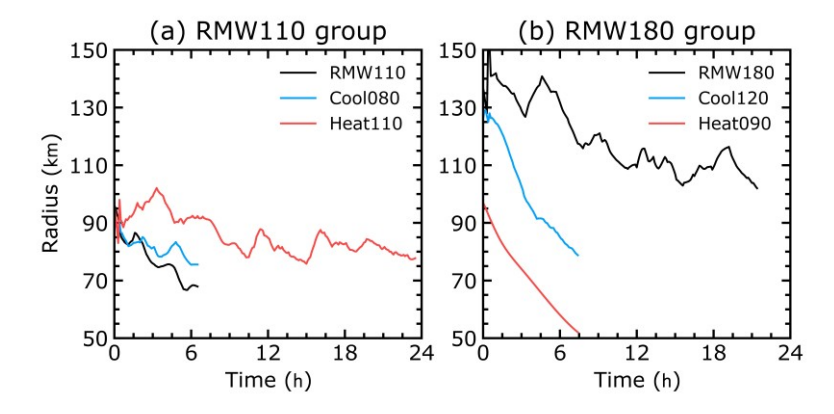


Figure 14. Temporal evolutions of radii of maximum azimuthally averaged 10-m-height tangential wind speeds near the outer eyewalls of TCs in (a) the RMW110 group, and (b) the RMW180 group.

In brief, we find that a TC with active outer rainbands is more likely to have a longer ERC timescale. Interestingly, spiral rainbands are also considered to be important for triggering the SEF (Didlake & Houze, 2013; Wang & Tan, 2020; Yu & Didlake, 2019; Yu et al., 2022; Yu et al., 2021). Based on the results in this study, we suggest that active rainbands can not only facilitate the generation of the secondary eyewall but also extend the maintenance of concentric eyewall structures by producing a vertically tilted and slowly contracting outer eyewall. This implies that the role of spiral rainbands is not only limited to the early phase of the ERC but also involved in the subsequent evolution of the concentric eyewall structure. Another interesting finding is that active rainbands are likely to induce a larger and wider outer convective ring (Figure 10), which was previously documented in single-eyewall TCs by Wang (2009). It seems that the significant relationship between the moat width and the outer eyewall width, reported in the observation-based study by Yang et al. (2021), is largely controlled by the activity of outer spiral rainbands. This could be a good topic for a future study.

5. Conclusions and discussion

Observational studies have shown that the concentric eyewall duration is significantly correlated with the moat width, which is rendered as a key ingredient that can regulate the interaction between inner and outer eyewalls. In this study, we have emphasized the important role of boundary layer dynamics in leading to the demise of the inner eyewall and the relationship between moat width and weakening rate. We used the three-layer Ooyama-type model (OM3L) and the nonhydrostatic, full-physics cloud model CM1 to address this issue. According to the backward trajectory analysis of Tsujino et al. (2017), the largest amount of air parcels arriving at the outer edge of the inner eyewall in the boundary layer have followed a path that is oriented radially inward, which can be perfectly manifested by the inflow diagnostic equations derived by Wang et al. (2013) (Eq. 3 and Eq. 4). Based on the equations, the inflow intensity near the inner eyewall is determined by the radial velocity at the outermost edge of the moat and the velocity increment within the moat.

Results show that the radial speed at the inner edge of the outer eyewall remains relatively identical during the development of the secondary eyewall and among experiments, although the reduction of the inflow intensity is proportional to the outer eyewall strength. Therefore, the acceleration process within the moat plays a more critical role in determining inflow strength in the inner-core region. The inflow budget shows that the net radial force (NRF) within the moat is primarily governed by the agradient force, friction and diffusion terms, which are mainly affected by the intensity of the inner eyewall. With respect to the same maximum wind speed near the inner eyewall, results from both simple and sophisticated full-physics models indicate that there would be stronger inflow reaching the inner eyewall with a larger moat due to a longer travelling distance for air parcels to accelerate. Thus, there is greater amount of radial flux of absolute vorticity, which can largely compensate the negative tangential wind tendency induced by the friction, diffusion, and vertical advection, based on the tangential wind budget in the boundary layer.

Previous studies suggested the interception of moist entropy by the outer eyewall has a salient contribution to the collapse of the inner eyewall. However, we have shown that the weakening of the inner eyewall is not always accompanied by the decrease in equivalent potential temperature (θ_e) in the inner-core region in the boundary layer. Results from the θ_e budget indicate that surface enthalpy flux and upward advection of moisture in the inner eyewall are sufficient to overcome local unfavorable condition resulting from the radial advection of low- θ_e air and lower

atmospheric warming. This implies that the boundary layer thermodynamic processes are not required in the demise of the inner eyewall in our simulations, with a notion in mind that we are not denying the influences of thermodynamic processes but arguing they are not indispensable to the inner eyewall decay. Overall, our findings support the theoretical hypothesis of Kuo et al. (2022), who proposed that the steady-state inner eyewall updraft scaled with the RMW is determined by the dimensionless moat width that is scaled with the Rossby deformation radius, using a slab boundary layer model. The direct connection between the weakening rate of the inner eyewall and the moat width is also consistent with observations (Yang et al., 2013; Yang et al., 2021).

Since the moat width can determine the amount of angular momentum transported into the inner eyewall, it is of special interest to figure out what processes can impact the change of the moat width or the contraction of the outer eyewall. We have revealed that active outer rainbands can promote the outer eyewall to form at a larger radius and result in a slower contraction rate of the outer eyewall. As suggested by Wang (2009) for a single-eyewall TC that active convective activity in outer rainbands tends to generate a large eye and an outwardly tilted eyewall, we find that the radial location and structure of the outer eyewall are subject to similar modulation by outer rainbands in a double-eyewall TC as well. In the experiments with artificially increased diabatic heating or reduced diabatic cooling rate in the outer region, outwardly tilted vertical structure of the outer eyewall and active outer rainbands induce relatively smaller (larger) tangential wind tendency on the inner (outer) side of the outer eyewall. As a result, the outer eyewall contracts inward at a smaller rate, and inner eyewall can survive longer. This implies that TCs with active outer rainbands are likely to have long-lasting concentric eyewall structure after the SEF. In addition, we notice that TCs with enhanced outer convection tend to have a tilted, large and wide outer eyewall. The connection between the moat width and the outer eyewall width has been reported in a statistical study by Yang et al. (2021).

In this study, we have interpreted the ERC timescale from the axisymmetric viewpoint. However, asymmetric characteristics exist in the outer eyewall since the time when outer spiral rainbands give birth to it. The eddy transport of angular momentum or thermodynamic scalars can have a nonnegligible contribution to the eyewall replacement. Therefore, a comprehensive study to elaborate both the axisymmetric and asymmetric aspects will be a topic in our future work.

- 753 **Acknowledgments**: This study was supported partly by the National Key R&D Program of China
- under grant 2022YFC3004200 and partly by S&T Development Fund of CAMS (2024KJ017). YW
- 755 was supported by NSF grant AGS-1834300.
- 756 **Data Availability Statement:** The CM1 source code was downloaded from the website:
- 757 https://www2.mmm.ucar.edu/people/bryan/cm1/. The model data produced in this article are
- 758 publicly available from Jiang and Wang (2024).

References

- Abarca, S. F., & Corbosiero, K. L. (2011). Secondary eyewall formation in WRF simulati ons of Hurricanes Rita and Katrina (2005). *Geophysical Research Letters*, 38(7). https://doi.org/10.1029/2011GL047015
- Abarca, S. F., & Montgomery, M. T. (2013). Essential Dynamics of Secondary Eyewall F ormation. *Journal of the Atmospheric Sciences*, 70(10), 3216-3230. https://doi.org/10.1 175/JAS-D-12-0318.1
- Abarca, S. F., & Montgomery, M. T. (2014). Departures from Axisymmetric Balance Dyn amics during Secondary Eyewall Formation. *Journal of the Atmospheric Sciences*, 71 (10), 3723-3738. https://doi.org/10.1175/JAS-D-14-0018.1
- Abarca, S. F., & Montgomery, M. T. (2015). Are Eyewall Replacement Cycles Governed Largely by Axisymmetric Balance Dynamics? *Journal of the Atmospheric Sciences*, 7 2(1), 82-87. https://doi.org/10.1175/JAS-D-14-0151.1
- Abarca, S. F., Montgomery, M. T., & McWilliams, J. C. (2015). The azimuthally average d boundary layer structure of a numerically simulated major hurricane. *Journal of Ad vances in Modeling Earth Systems*, 7(3), 1207-1219. https://doi.org/10.1002/2015MS00 0457
- Ahern, K., Hart, R. E., & Bourassa, M. A. (2022). Asymmetric Hurricane Boundary Laye r Structure during Storm Decay. Part II: Secondary Eyewall Formation. *Monthly Weat* her Review, 150(8), 1915-1936. https://doi.org/10.1175/MWR-D-21-0247.1
- Black, M. L., & Willoughby, H. E. (1992). The Concentric Eyewall Cycle of <u>Hurricane</u> G ilbert. *Monthly Weather Review*, *120*(6), 947-957. <a href="https://doi.org/10.1175/1520-0493(199-2)120<0947:TCECOH>2.0.CO;2">https://doi.org/10.1175/1520-0493(199-2)120<0947:TCECOH>2.0.CO;2
- Bryan, G. H., & Rotunno, R. (2009). The Maximum Intensity of Tropical Cyclones in A xisymmetric Numerical Model Simulations. *Monthly Weather Review*, 137(6), 1770-17 89. https://doi.org/10.1175/2008MWR2709.1
- Chen, G. (2018). Secondary Eyewall Formation and Concentric Eyewall Replacement in Association with Increased Low-Level Inner-Core Diabatic Cooling. *Journal of the At* mospheric Sciences, 75(8), 2659-2685. https://doi.org/10.1175/JAS-D-17-0207.1
- Chen, X., Rozoff, C. M., Rogers, R. F., Corbosiero, K. L., Tao, D., Gu, J.-F., Judt, F., H endricks, E. A., Wang, Y., Bell, M. M., Stern, D. P., Musgrave, K. D., Knaff, J. A.,

- 8 Kaplan, J. (2023). Research advances on internal processes affecting tropical cycl one intensity change from 2018–2022. *Tropical Cyclone Research and Review*, 12(1), 10-29. https://doi.org/10.1016/j.tcrr.2023.05.001
- Didlake, A. C., & Houze, R. A. (2013). Dynamics of the Stratiform Sector of a Tropical Cyclone Rainband. *Journal of the Atmospheric Sciences*, 70(7), 1891-1911. https://doi.org/10.1175/JAS-D-12-0245.1
- Dunion, J. P. (2011). Rewriting the Climatology of the Tropical North Atlantic and Carib bean Sea Atmosphere. *Journal of Climate*, 24(3), 893-908. https://doi.org/10.1175/2010
 JCLI3496.1
- Fei, R., & Wang, Y. (2021). Tropical Cyclone Intensification Simulated in the Ooyama-Ty pe Three-Layer Model with a Multilevel Boundary Layer. *Journal of the Atmospheric Sciences*, 78(11), 3799-3813. https://doi.org/10.1175/JAS-D-21-0127.1
- Fortner, L. E. (1958). Typhoon Sarah, 1956. *Bulletin of the American Meteorological Soci* ety, 39(12), 633-639. https://doi.org/10.1175/1520-0477-39.12.633

805 806

807 808

809

- Hawkins, J., Helveston, M., Lee, T., Turk, J., Richardson, K., Sampson, C., Kent, J., & Wade, R. (2006, 01/01). Tropical cyclone multiple eyewall characteristics. In *Reprints*, 27th conf. On Hurricane and tropical Meteorology. Amer. Meteor. Soc. 6B.1. Retriev ed from http://ams.confex.com/ams/27Hurricanes/techprogram/paper 108864.htm
 - Hawkins, J. D. (2008). Tropical cyclone multiple eyewall characteristics. In *28th conference* on hurricanes and tropical Meteorology. Amer. Meteor. Soc. 6B.1. Retrieved from <u>h</u> ttp://ams.confex.com/ams/28Hurricanes/techprogram/paper_138300.htm
- Hawkins, J. D., & Helveston, M. (2004). Tropical cyclone multiple eyewall characteristics. In *Prepints*, *26th Conf. on Hurricanes and Tropical Meteorology*. Amer. Meteor. Soc. Retrieved from https://ams.confex.com/ams/26HURR/techprogram/paper 76084.htm
- Houze, R. A., Chen, S. S., Smull, B. F., Lee, W.-C., & Bell, M. M. (2007). Hurricane I ntensity and Eyewall Replacement. *Science*, *315*(5816), 1235-1239. 10.1126/science.11 35650. https://www.science.org/doi/10.1126/science.1135650
- Huang, Y.-H., Montgomery, M. T., & Wu, C.-C. (2012). Concentric Eyewall Formation in Typhoon Sinlaku (2008). Part II: Axisymmetric Dynamical Processes. *Journal of the* Atmospheric Sciences, 69(2), 662-674. https://doi.org/10.1175/JAS-D-11-0114.1
- Irish, J. L., Resio, D. T., & Ratcliff, J. J. (2008). The Influence of Storm Size on Hurric ane Surge. *Journal of Physical Oceanography*, 38(9), 2003-2013. https://doi.org/10.117
 822

 5/2008JPO3727.1
- Jiang, J., & Wang, Y. (2024). The Roles of Moat Width and Outer Eyewall Contraction i n affecting the Timescale of Eyewall Replacement Cycle [Dataset]. *Dryad*. https://datadryad.org/stash/share/tUgrxzXhk82iGJLc5nwd62O9Z6iPWDM3Q WtqKSWPd8
- Kepert, J. D. (2010a). Slab- and height-resolving models of the tropical cyclone boundary layer. Part I: Comparing the simulations. *Quarterly Journal of the Royal Meteorolog ical Society*, 136(652), 1686-1699. https://doi.org/10.1002/qj.667
- Kepert, J. D. (2010b). Slab- and height-resolving models of the tropical cyclone boundary layer. Part II: Why the simulations differ. *Quarterly Journal of the Royal Meteorolo*

- 831 gical Society, 136(652), 1700-1711. https://doi.org/10.1002/qj.685
- Kepert, J. D. (2013). How Does the Boundary Layer Contribute to Eyewall Replacement
 Cycles in Axisymmetric Tropical Cyclones? *Journal of the Atmospheric Sciences*, 70
 (9), 2808-2830. https://doi.org/10.1175/JAS-D-13-046.1
- Kepert, J. D., & Nolan, D. S. (2014). Reply to "Comments on 'How Does the Boundary Layer Contribute to Eyewall Replacement Cycles in Axisymmetric Tropical Cyclone s?". *Journal of the Atmospheric Sciences*, 71(12), 4692-4704. https://doi.org/10.1175/J
 AS-D-14-0014.1
- Kepert, J. D. (2017). Time and Space Scales in the Tropical Cyclone Boundary Layer, an d the Location of the Eyewall Updraft. *Journal of the Atmospheric Sciences*, 74(10), 3305-3323. https://doi.org/10.1175/JAS-D-17-0077.1
- Kossin, J. P., Schubert, W. H., & Montgomery, M. T. (2000). Unstable Interactions betwe en a Hurricane's Primary Eyewall and a Secondary Ring of Enhanced Vorticity. *Jour* nal of the Atmospheric Sciences, 57(24), 3893-3917. https://doi.org/10.1175/1520-0469 (2001)058<3893:UIBAHS>2.0.CO;2
- Kossin, J. P., & Sitkowski, M. (2009). An Objective Model for Identifying Secondary Ey ewall Formation in Hurricanes. *Monthly Weather Review*, 137(3), 876-892. https://doi.org/10.1175/2008MWR2701.1
- Kuo, H.-C., Chang, C.-P., Yang, Y.-T., & Jiang, H.-J. (2009). Western North Pacific Typh oons with Concentric Eyewalls. *Monthly Weather Review*, 137(11), 3758-3770. https://doi.org/10.1175/2009MWR2850.1
- Kuo, H.-C., Schubert, W. H., Tsai, C.-L., & Kuo, Y.-F. (2008). Vortex Interactions and B arotropic Aspects of Concentric Eyewall Formation. *Monthly Weather Review*, 136(12), 5183-5198. https://doi.org/10.1175/2008MWR2378.1
- Kuo, H.-C., Tsujino, S., Hsu, T.-Y., Peng, M. S., & Su, S.-H. (2022). Scaling Law for B oundary Layer Inner Eyewall Pumping in Concentric Eyewalls. *Journal of Geophysic al Research: Atmospheres*, 127(4), e2021JD035518. https://doi.org/10.1029/2021JD0355
 18
- Kuo, H. C., Lin, L. Y., Chang, C. P., & Williams, R. T. (2004). The Formation of Conc entric Vorticity Structures in Typhoons. *Journal of the Atmospheric Sciences*, 61(22), 2722-2734. https://doi.org/10.1175/JAS3286.1
- Lai, T.-K., Hendricks, E. A., Menelaou, K., & Yau, M. K. (2021). Roles of Barotropic In stability across the Moat in Inner Eyewall Decay and Outer Eyewall Intensification:

 Three-Dimensional Numerical Experiments. *Journal of the Atmospheric Sciences*, 78 (2), 473-496. https://doi.org/10.1175/JAS-D-20-0168.1
- Lai, T.-K., Hendricks, E. A., & Yau, M. K. (2021). Long-Term Effect of Barotropic Insta bility across the Moat in Double-Eyewall Tropical Cyclone–Like Vortices in Forced a nd Unforced Shallow-Water Models. *Journal of the Atmospheric Sciences*, 78(12), 41 03-4126. https://doi.org/10.1175/JAS-D-21-0065.1
- Lai, T.-K., Hendricks, E. A., Yau, M. K., & Menelaou, K. (2021). Roles of Barotropic In stability across the Moat in Inner Eyewall Decay and Outer Eyewall Intensification:

- Essential Dynamics. *Journal of the Atmospheric Sciences*, 78(5), 1411-1428. https://doi.org/10.1175/JAS-D-20-0169.1
- Lai, T.-K., Menelaou, K., & Yau, M. K. (2019). Barotropic Instability across the Moat an d Inner Eyewall Dissipation: A Numerical Study of Hurricane Wilma (2005). *Journal of the Atmospheric Sciences*, 76(4), 989-1013. https://doi.org/10.1175/JAS-D-18-0191.
- Li, Y., Wang, Y., & Lin, Y. (2019). Revisiting the Dynamics of Eyewall Contraction of Tropical Cyclones. *Journal of the Atmospheric Sciences*, 76(10), 3229-3245. https://doi.org/10.1175/JAS-D-19-0076.1
- Li, Y., Wang, Y., Lin, Y., & Wang, X. (2021). Why Does Rapid Contraction of the Radi us of Maximum Wind Precede Rapid Intensification in Tropical Cyclones? *Journal of the Atmospheric Sciences*, 78(11), 3441-3453. https://doi.org/10.1175/JAS-D-21-0129.1

885

886

887

902

903

904

- Lin, N., Lane, P., Emanuel, K. A., Sullivan, R. M., & Donnelly, J. P. (2014). Heightened hurricane surge risk in northwest Florida revealed from climatological-hydrodynamic modeling and paleorecord reconstruction. *Journal of Geophysical Research: Atmospher es*, 119(14), 8606-8623. https://doi.org/10.1002/2014JD021584
- McNoldy, B. D. (2004). Triple Eyewall in Hurricane Juliette. *Bulletin of the American M* eteorological Society, 85(11), 1663-1666. https://doi.org/10.1175/bams-85-11-1663
- Molinari, J., Zhang, J. A., Rogers, R. F., & Vollaro, D. (2019). Repeated Eyewall Replac ement Cycles in Hurricane Frances (2004). *Monthly Weather Review*, 147(6), 2009-20 22. https://doi.org/10.1175/MWR-D-18-0345.1
- 893 Ooyama, K. (1969). Numerical Simulation of the Life Cycle of Tropical Cyclones. *Journa*894 *l of Atmospheric Sciences*, 26(1), 3-40. <a href="https://doi.org/10.1175/1520-0469(1969)026<00">https://doi.org/10.1175/1520-0469(1969)026<00
 895 03:NSOTLC>2.0.CO;2
- Qiu, X., Tan, Z.-M., & Xiao, Q. (2010). The Roles of Vortex Rossby Waves in Hurrican e Secondary Eyewall Formation. *Monthly Weather Review*, 138(6), 2092-2109. https://doi.org/10.1175/2010MWR3161.1
- Rostami, M., & Zeitlin, V. (2022). Evolution of double-eye wall hurricanes and emergenc e of complex tripolar end states in moist-convective rotating shallow water model. *P* hysics of Fluids, 34(6), 066602. 10.1063/5.0096554
 - Rotunno, R., & Emanuel, K. A. (1987). An Air–Sea Interaction Theory for Tropical Cycl ones. Part II: Evolutionary Study Using a Nonhydrostatic Axisymmetric Numerical M odel. *Journal of Atmospheric Sciences*, 44(3), 542-561. <a href="https://doi.org/10.1175/1520-0469(1987)044<0542:AAITFT>2.0.CO;2">https://doi.org/10.1175/1520-0469(1987)044<0542:AAITFT>2.0.CO;2
- Rozoff, C. M., Schubert, W. H., & Kossin, J. P. (2008). Some dynamical aspects of tropi cal cyclone concentric eyewalls. *Quarterly Journal of the Royal Meteorological Societ y*, 134(632), 583-593. https://doi.org/10.1002/qj.237
- Rozoff, C. M., Schubert, W. H., McNoldy, B. D., & Kossin, J. P. (2006). Rapid Filament ation Zones in Intense Tropical Cyclones. *Journal of the Atmospheric Sciences*, 63(1), 325-340. https://doi.org/10.1175/JAS3595.1
- 912 Samsury, C. E., & Zipser, E. J. (1995). Secondary Wind Maxima in Hurricanes: Airflow

- 913 and Relationship to Rainbands. *Monthly Weather Review*, *123*(12), 3502-3517. <a href="https://doi.org/10.1175/1520-0493(1995)123<3502:SWMIHA>2.0.CO;2">https://doi.org/10.1175/1520-0493(1995)123<3502:SWMIHA>2.0.CO;2
- 915 Schecter, D. A., & Dunkerton, T. J. (2009). Hurricane formation in diabatic Ekman turbul 916 ence. *Quarterly Journal of the Royal Meteorological Society*, 135(641), 823-838. https://doi.org/10.1002/qj.405
- 918 Shapiro, L. J., & Willoughby, H. E. (1982). The Response of Balanced Hurricanes to Lo 919 cal Sources of Heat and Momentum. *Journal of Atmospheric Sciences*, 39(2), 378-39 920 4. <a href="https://doi.org/10.1175/1520-0469(1982)039<0378:TROBHT>2.0.CO;2">https://doi.org/10.1175/1520-0469(1982)039<0378:TROBHT>2.0.CO;2
- 921 Sitkowski, M., Kossin, J. P., & Rozoff, C. M. (2011). Intensity and Structure Changes du 922 ring Hurricane Eyewall Replacement Cycles. *Monthly Weather Review*, 139(12), 3829-923 3847. https://doi.org/10.1175/MWR-D-11-00034.1
- 924 Slocum, C. J., Taft, R. K., Kossin, J. P., & Schubert, W. H. (2023). Barotropic Instability 925 during Eyewall Replacement. *Meteorology*, 2(2), 191-221. https://www.mdpi.com/2674 926 -0494/2/2/13
- 927 Stern, D. P., Vigh, J. L., Nolan, D. S., & Zhang, F. (2015). Revisiting the Relationship b 928 etween Eyewall Contraction and Intensification. *Journal of the Atmospheric Sciences*, 929 72(4), 1283-1306. https://doi.org/10.1175/JAS-D-14-0261.1
- Terwey, W. D., & Montgomery, M. T. (2008). Secondary eyewall formation in two ideali zed, full-physics modeled hurricanes. *Journal of Geophysical Research: Atmospheres*, 113(D12). https://doi.org/10.1029/2007JD008897

934

935

- Thompson, G., Field, P. R., Rasmussen, R. M., & Hall, W. D. (2008). Explicit Forecasts of Winter Precipitation Using an Improved Bulk Microphysics Scheme. Part II: Imple mentation of a New Snow Parameterization. *Monthly Weather Review*, 136(12), 5095-5115. https://doi.org/10.1175/2008MWR2387.1
- Tsujino, S., Tsuboki, K., & Kuo, H.-C. (2017). Structure and Maintenance Mechanism of Long-Lived Concentric Eyewalls Associated with Simulated Typhoon Bolaven (2012).

 Journal of the Atmospheric Sciences, 74(11), 3609-3634. https://doi.org/10.1175/JAS-D
 16-0236.1
- Tsujino, S., Horinouchi, T., Tsukada, T., Kuo, H. C., Yamada, H., & Tsuboki, K. (2021).

 Inner-Core Wind Field in a Concentric Eyewall Replacement of Typhoon Trami (201
 8): A Quantitative Analysis Based on the Himawari-8 Satellite. *Journal of Geophysic*al Research: Atmospheres, 126(7), e2020JD034434. https://doi.org/10.1029/2020JD0344
 34
- Wang, H., Yu, Y., Zhao, D., Yen, T.-H., Xu, H., Wang, Q., & Cao, Z. (2023). Unusual
 Evolution of the Multiple Eyewall Cycles in Super Typhoon Hinnamnor (2022). *Jour* nal of Meteorological Research, 37(4), 431-440. https://doi.org/10.1007/s13351-023-219
 3-8
- Wang, X., Ma, Y., & Davidson, N. E. (2013). Secondary Eyewall Formation and Eyewall Replacement Cycles in a Simulated Hurricane: Effect of the Net Radial Force in th e Hurricane Boundary Layer. *Journal of the Atmospheric Sciences*, 70(5), 1317-1341. https://doi.org/10.1175/JAS-D-12-017.1

- Wang, Y.-F., & Tan, Z.-M. (2020). Outer Rainbands–Driven Secondary Eyewall Formation of Tropical Cyclones. *Journal of the Atmospheric Sciences*, 77(6), 2217-2236. https://doi.org/10.1175/JAS-D-19-0304.1
- 957 Wang, Y. (2008). Rapid Filamentation Zone in a Numerically Simulated Tropical Cyclone.
 958 *Journal of the Atmospheric Sciences*, 65(4), 1158-1181. https://doi.org/10.1175/2007J
 959 AS2426.1
- Wang, Y. (2009). How Do Outer Spiral Rainbands Affect Tropical Cyclone Structure and
 Intensity? *Journal of the Atmospheric Sciences*, 66(5), 1250-1273. https://doi.org/10.11
 75/2008JAS2737.1
- 963 Willoughby, H. E. (1990). Gradient Balance in Tropical Cyclones. *Journal of Atmospheric* 964 Sciences, 47(2), 265-274. <a href="https://doi.org/10.1175/1520-0469(1990)047<0265:GBITC>2.0.C">https://doi.org/10.1175/1520-0469(1990)047<0265:GBITC>2.0.C 965 O;2
- Willoughby, H. E., Clos, J. A., & Shoreibah, M. G. (1982). Concentric Eye Walls, Secon dary Wind Maxima, and The Evolution of the Hurricane vortex. *Journal of Atmosphe ric Sciences*, 39(2), 395-411. https://doi.org/10.1175/1520-0469(1982)039
 WM>2.0.CO;2
- 970 Wu, C.-C., Huang, Y.-H., & Lien, G.-Y. (2012). Concentric Eyewall Formation in Typhoo 971 n Sinlaku (2008). Part I: Assimilation of T-PARC Data Based on the Ensemble Kal 972 man Filter (EnKF). *Monthly Weather Review*, 140(2), 506-527. https://doi.org/10.1175/MWR-D-11-00057.1
- Xu, J., & Wang, Y. (2010a). Sensitivity of the Simulated Tropical Cyclone Inner-Core Siz
 e to the Initial Vortex Size. *Monthly Weather Review*, 138(11), 4135-4157. https://doi.org/10.1175/2010MWR3335.1
- Xu, J., & Wang, Y. (2010b). Sensitivity of Tropical Cyclone Inner-Core Size and Intensit
 y to the Radial Distribution of Surface Entropy Flux. *Journal of the Atmospheric Sci* ences, 67(6), 1831-1852. https://doi.org/10.1175/2010JAS3387.1
- Yang, X.-W., Wang, Y., Wang, H., Xu, J., and Zhan, R.-F. (2024). Effect of the initial v ortex structure on intensity change during eyewall replacement cycle of tropical cyclo nes: A numerical study. *Journal of Tropical Meteorology*, (in press). https://doi.org/10.3724/j.1006-8775.2024.011
- 984 Yang, Y.-T., Hendricks, E. A., Kuo, H.-C., & Peng, M. S. (2014). Long-Lived Concentric 985 Eyewalls in Typhoon Soulik (2013). *Monthly Weather Review*, 142(9), 3365-3371. https://doi.org/10.1175/MWR-D-14-00085.1
- 987 Yang, Y.-T., Kuo, H.-C., Hendricks, E. A., & Peng, M. S. (2013). Structural and Intensit 988 y Changes of Concentric Eyewall Typhoons in the Western North Pacific Basin. *Mon* 989 thly Weather Review, 141(8), 2632-2648. https://doi.org/10.1175/MWR-D-12-00251.1
- 990 Yang, Y.-T., Kuo, H.-C., Tsujino, S., Chen, B.-F., & Peng, M. S. (2021). Characteristics o 991 f the Long-Lived Concentric Eyewalls in Tropical Cyclones. *Journal of Geophysical* 992 *Research: Atmospheres*, 126(11), e2020JD033703. https://doi.org/10.1029/2020JD033703
- 993 Yu, C.-L., & Didlake, A. C. (2019). Impact of Stratiform Rainband Heating on the Tropi cal Cyclone Wind Field in Idealized Simulations. *Journal of the Atmospheric Science*

- 995 s, 76(8), 2443-2462. <u>https://doi.org/10.1175/JAS-D-18-0335.1</u>
- 996 Yu, C.-L., Didlake, A. C., & Zhang, F. (2022). Updraft Maintenance and Axisymmetrizati 997 on during Secondary Eyewall Formation in a Model Simulation of Hurricane Matthe 998 w (2016). *Journal of the Atmospheric Sciences*, 79(4), 1105-1125. https://doi.org/10.11 999 75/JAS-D-21-0103.1
- Yu, C.-L., Didlake Jr, A. C., Kepert, J. D., & Zhang, F. (2021). Investigating Axisymmet ric and Asymmetric Signals of Secondary Eyewall Formation Using Observations-Bas ed Modeling of the Tropical Cyclone Boundary Layer. *Journal of Geophysical Resea rch: Atmospheres*, 126(16), e2020JD034027. https://doi.org/10.1029/2020JD034027
- Zhao, K., Lin, Q., Lee, W.-C., Qiang Sun, Y., & Zhang, F. (2016). Doppler Radar Analy sis of Triple Eyewalls in Typhoon Usagi (2013). *Bulletin of the American Meteorolo gical Society*, 97(1), 25-30. https://doi.org/10.1175/BAMS-D-15-00029.1
- Zhou, X., & Wang, B. (2011). Mechanism of Concentric Eyewall Replacement Cycles an d Associated Intensity Change. *Journal of the Atmospheric Sciences*, 68(5), 972-988. https://doi.org/10.1175/2011JAS3575.1
- Zhou, X., Wang, B., Ge, X., & Li, T. (2011). Impact of Secondary Eyewall Heating on Tropical Cyclone Intensity Change. *Journal of the Atmospheric Sciences*, 68(3), 450-4 56. https://doi.org/10.1175/2010JAS3624.1
- Zhu, X.-S., & Yu, H. (2019). Environmental Influences on the Intensity and Configuration of Tropical Cyclone Concentric Eyewalls in the Western North Pacific. *Journal of t he Meteorological Society of Japan. Ser. II*, 97(1), 153-173. https://doi.org/10.2151/jms1016
- Zhu, Z., & Zhu, P. (2014). The role of outer rainband convection in governing the eyew all replacement cycle in numerical simulations of tropical cyclones. *Journal of Geoph ysical Research: Atmospheres*, 119(13), 8049-8072. https://doi.org/10.1002/2014JD0218